Detection and Analysis of Partial Discharges in Non-uniform Field

by

Longfei Cui

A Thesis Presented in Partial Fulfillment
of the Requirements for the Degree
Master of Science

Approved November 2013 by the
Graduate Supervisory Committee:

Ravi Gorur, Chair
Vijay Vittal
Raja Ayyanar

ARIZONA STATE UNIVERSITY

May 2014

ABSTRACT

Insulation aging monitoring is widely used to evaluate the operating condition of power equipment. One important monitoring method is detecting partial discharges (PD). PD is a localized breakdown of dielectric and its characteristics can give information about the insulation aging. Most existing test methods cannot identify different kinds of defects. Also, the practical application of PD detection in most existing test methods is restricted by weak PD signals and strong electric field disturbance from surroundings.

In order to monitor aging situation in detail, types of PDs are important features to take into account. To classify different types of PDs, pulse sequence analysis (PSA) method is advocated to analyze PDs in the rod-plane model. This method can reflect cumulative effects of PDs, which are always ignored when only measuring PD value. It also shows uniform characteristics when different kinds of detecting system are utilized. Moreover, it does not need calibration. Analysis results from PSA show highly consistent distribution patterns for the same type of PDs and significant differences in the distribution patterns among types of PDs.

Furthermore, a new method to detect PD signals using fiber bragg grating (FBG) based PD sensor is studied in this research. By using a piezoelectric ceramic transducer (PZT), small PD signals can be converted to pressure signal and then converted to an optical wavelength signal with FBG. The optical signal is isolated from the electric field; therefore its attenuation and anti-jamming performance will be better than traditional methods. Two sensors, one with resonant frequency of 42.7 kHz and the other 300 kHz, were used to explore the performance of this testing system. However, there were issues with the sensitivity of the sensors of these devices and the results have been

communicated with the company. These devices could not give the results at the same level of accuracy as the conventional methods.

ACKNOWLEDGEMENTS

Firstly, I would like to sincerely offer my gratitude and respect to my advisor Dr. Ravi Gorur, whose support and guidance have enabled me to work on this project and finish the thesis. I also would like to thank my committee members, Dr. Vijay Vittal and Dr. Raja Ayyanar, for their time and advice.

Secondly, I want to acknowledge Intelligent Fiber Optic Systems (IFOS) for their sample and equipment, as well as their funding towards this thesis.

Finally, I am especially grateful for my family and friends for always standing by me.

TABLE OF CONTENTS

Page

LIST OF TABLES vii

LIST OF FIGURES viii

Chapter 1 INTRODUCTION 1

1.1 Introduction and Background 1

1.2 Research Objectives 2

1.3 Organization and Content 3

Chapter 2 LITERATURE REVIEW ON DISCHARGES 5

2.1 Detection Methods 5

2.1.1 Electrical Methods 5

2.1.2 Non-electrical Methods 6

2.2 Analysis Methods 8

Chapter 3 DISCHARGE STUDY WITH CONVENTIONAL METHOD 9

3.1 Introduction 9

3.2 Methods of Data Analysis 9

3.2.1 The Analysis of Variance 9

3.2.2 Time-Frequency Map 10

3.3 Experiment System 12

3.3.1 System Diagram 12

3.3.2 Calibration 13

3.4 ANOVA Analysis 13

3.4.1 Relation between PD value and Voltage 14

Page

3.4.2 Relation between PD value and Rod Diameter....14
3.4.3 Relation between PD value and Gap Distance....15
3.4.4 Analysis of Data....16
3.5 Time-Frequency Analysis....17
3.5.1 Differences among Rod Diameters....17
3.5.2 Differences among Gap Distances....18
3.5.3 Differences among Voltages....19
3.5.4 Differences among Different Types of Discharges....20
3.6 Discussion....21
Chapter 4 STUDY OF ROD-PLANE MODEL WITH PULSE SEQUENCE ANALYSIS METHOD....23
4.1 Introduction....23
4.2 Experiment Theory....23
4.2.1 Pulse Sequence Analysis Method....23
4.2.2 Simulation of Rod-Plane Model....24
4.3 System Setup....27
4.4 Tests and Results....27
4.4.1 $\Delta u/\Delta\varphi$ Graph....28
4.4.2 $\Delta u(i+1)/\Delta u(i)$ Graph....31
4.4.3 Discussion....34
Chapter 5 EXPERIMENT WITH FBG-BASED PD SENSOR....35
5.1 Introduction....35

Page

5.2 Experiment Theory 35
5.2.1 PDs in Cable 35
5.2.2 FBG-based PD Sensor 36
5.2.3 Simulation of Cable 36
5.3 Experiment System 40
5.4 Pre-Test of Cable 41
5.5 Tests and Results 42
5.5.1 Test with 42.7 kHz PD Sensor 42
5.5.2 Sensor's Response to Impulse 56
5.5.3 Test with 300 kHz PD Sensor 62
5.5.4 Discussion 65
Chapter 6 CONCLUSIONS AND FUTURE WORK 66
6.1 Conclusions 66
6.2 Future Work 67
REFERENCES 69

LIST OF TABLES

Table Page

1. Levels of Three Factors..... 14

2. ANOVA Table for PD Value 17

3. Electric Field for 0.91 mm Rod Diameter 26

4. Electric Field for 18 mm Gap Distance 26

5. Parameters of Rod Diameters and Gap Distances 28

6. Test Results 42

7. RMS and P-P Values with IIR Filter..... 55

8. RMS and P-P Values without Electronics..... 56

9. RMS and P-P Values without 1MHz Interrogator..... 56

10. RMS and P-P Values before IIR Filter..... 62

11. RMS and P-P Values after IIR Filter..... 63

12. RMS and P-P Values from Oscilloscope without IIR Filter 63

13. RMS and P-P Values from Oscilloscope with IIR Filter..... 64

LIST OF FIGURES

Figure Page

1. Conventional Test System 5

2. System Diagram 12

3. Coupling Quadripole 13

4. pC /V when D=0.91 mm 14

5. pC /V when D=1.58 mm 14

6. pC /V when D=01.96 mm 14

7. pC /V when D=2.36 mm 14

8. pC /D when G=22 mm 15

9. pC /D when G=20 mm 15

10. pC /D when G=18 mm 15

11. pC /D when G=16 mm 15

12. pC /G when V=10 kV 16

13. pC /G when V=11 kV 16

14. pC /G when V=12 kV 16

15. pC /G when V=13 kV 16

16. pC/G when V=14 kV 16

17. TF Map for D=2.98 mm 18

18. TF Map for D=2.36 mm 18

19. TF Map for D=1.96 mm 18

20. TF Map for D=1.58 mm 18

21. TF Map for G=22 mm 19

Figure Page

22. TF Map for G=20 mm 19

23. TF Map for G=18 mm 19

24. TF Map for G=16 mm 19

25. TF Map for V=14.4 kV 20

26. TF Map for V=13.2 kV 20

27. TF Map for V=12 kV 20

28. TF Map for V=10.8 kV 20

29. TF Map for Rod-Plane Model 21

30. TF Map for Cable 21

31. TF Map for Rod-Rod Model in Epoxy 21

32. Definition of Voltage and Phase Changes [32] 24

33. Simulation Model 25

34. Electric Field Distribution for 0.91 mm Rod Diameter 25

35. Electric Field Distribution for 18 mm Gap Distance 26

36. System Diagram 27

37. Two Types of PDs 28

38. D=2.36mm and G=18 mm 28

39. D=2.36 mm and G=20 mm 28

40. D=2.36 mm and G=22 mm 29

41. D=2.36 mm and G=24 mm 29

42. D=0.91 mm and G=24 mm 29

43. D=1.58 mm and G=24 mm 29

Figure Page

44. D=1.96 mm and G=24 mm 29

45. D=2.36 mm and G=24 mm 29

46. D=2.36 mm and G=18 mm 30

47. D=2.36 mm and G=20 mm 30

48. D=2.36 mm and G=22 mm 30

49. D=2.36 mm and G=24 mm 30

50. D=0.91 mm and G=24 mm 30

51. D=1.58 mm and G=24 mm 30

52. D=1.96 mm and G=24 mm 31

53. D=2.36 mm and G=24 mm 31

54. D=2.36 mm and G=18 mm 31

55. D=2.36 mm and G=20 mm 31

56. D=2.36 mm and G=22 mm 31

57. D=2.36 mm and G=24 mm 31

58. D=0.91 mm and G=24 mm 32

59. D=1.58 mm and G=24 mm 32

60. D=1.96 mm and G=24 mm 32

61. D=2.36 mm and G=24 mm 32

62. D=2.36 mm and G=18 mm 33

63. D=2.36 mm and G=20 mm 33

64. D=2.36 mm and G=22 mm 33

65. D=2.36 mm and G=24 mm 33

Figure Page

66. D=0.91 mm and G=24 mm 33

67. D=1.58 mm and G=24 mm 33

68. D=1.96 mm and G=24 mm 34

69. D=2.36 mm and G=24 m 34

70. Intact Cable Model 36

71. Electric Field of Intact Cable 37

72. Defective Cable Model 38

73. Electric Field of Defective Cable 38

74. Detail Distribution 39

75. Electric Field Distribution of Different Gaps 40

76. System Diagram for FBG-Based PD Sensor 40

77. Block Diagram for Detection System with FBG-based PD Sensor 41

78. Wavelength Waveform for 0 kV 43

79. FFT Result for 0 kV 43

80. Wavelength Waveform for 10 kV 44

81. FFT Result for 10 kV 44

82. Wavelength Waveform for 13 kV 45

83. FFT Result for 13 kV 45

84. Frequency Response of High Pass Filter 46

85. Wavelength Waveform for 0 kV 47

86. FFT Result for 0 kV 47

87. Wavelength Waveform for 5 kV 48

Figure Page

88. FFT Result for 5 kV 48

89. Wavelength Waveform for 13 kV 49

90. FFT Result for 13 kV 49

91. Frequency Rresponse of Band-Pass Filter 50

92. Wavelength Waveform for 0 kV 51

93. FFT Results for 0 kV 51

94. Wavelength Waveform for 5 kV 52

95. FFT Result for 5 kV 52

96. Wavelength Waveform for 13 kV 53

97. FFT Result for 13 kV 53

98. Frequency Response of IIR Filter 54

99. Wavelength Waveform for 0 kV 54

100. Wavelength Waveform for 5 kV 55

101. Wavelength Waveform for 13 kV 55

102. 1.1595 V Pulse Waveform 57

103. Real PD Signal in Cable 57

104. Wavelength Waveform for No Signal 57

105. FFT Result for No Signal 58

106. Wavelength Waveform for 0.11626 V Pulse 58

107. FFT Result for 0.11626 V Pulse 59

108. Wavelength Waveform for 0.28503 V Pulse 59

109. FFT Result for 0.28503 V Pulse 60

Figure Page

110. Wavelength Waveform for 0.57305 V Pulse 60

111. FFT Result for 0.57305 V Pulse 61

112. Wavelength Waveform for 1.1595 V Pulse 61

113. FFT Result for 1.1595 V Pulse 62

114. Magnitude Response for 300 kHz IIR Filter 63

115. High Magnitude Oscillation gotten by Oscilloscope 64

116. FFT Result for Oscillation under 15 kV 65

Chapter 1

INTRODUCTION

1.1 Introduction and Background

The ability to provide uninterrupted and reliable service to loads is imperative for the successful operation of power systems. Many disruptions in power systems are caused by failures of equipment, primarily due to insulation aging. Therefore, an effective way to evaluate insulation aging is necessary. PD, a temporary and localized breakdown of a small portion in dielectrics under high electric field, is widely used to evaluate insulation aging.

PD signals are generated when high non-uniform electric field is applied to defects in insulation materials. Several factors have influence on PD signals: location, size and geometry of defects [1]. As a result, for different defects, PD can occur with different intensities, phase positions and time intervals. These characteristics can reflect types of defects, which can be used to evaluate insulation aging, making PD signal analysis a practical way to monitor the situations. There are some limitations to PD detection that need improvement. Power equipment always runs under high electric field situation, and weak PD signals are easily drowned in the noise, such as environment electric field noise around the equipment, making them difficult to detect. Consequently, the detection of PD signals is as important as the analysis.

A proper PD analysis method is necessary to evaluate insulation aging, since PD signals contain abundant information of defects inside the insulation. Numerous studies have been conducted to analyze PD signals. PD is a random variable within a certain range [2], so distribution patterns are used to study it. Magnitude and phase distribution

are widely utilized to analyze PD signals. However, PDs have cumulative effects, which mean they are not isolated from each other [3]. For continuous PD phenomenon, each PD is affected by the previous one, an important characteristic ignored in magnitude and phase distribution. Also, due to the diversity of test system and tested equipment, those distributions are different, which means a new distribution database is necessary to be built for each new case.

Many detection methods have been studied and used to pick up PD signals (Please see Chapter 2 for review). These methods aim to improve the Signal-Noise Ratio (SNR) and detect PD signals sensitively. When PD happens, there is a current pulse, accompanied with sound, light and heat phenomena. Therefore, both electrical and non-electrical methods are used. On one hand, electrical methods perform well at detection sensitivity. But disturbance and attenuation are two main issues for testing systems [4]. On the other hand, non-electrical methods do not have such issues but face other problems. Non-electrical signals are very weak and hard to detect. Sometimes these signals attenuate to zero before reaching the insulation boundary, which makes them very hard to detect outside the insulation.

1.2 Research Objectives

This research focuses on new methods to detect and analyze PD signals. Pulse Sequence Analysis method is utilized to categorize different types of discharges in the Rod-Plane Model. In addition, a new detection system with FBG-based PD sensor is also used to explore a high-performance anti-jamming way of detecting PD signals. The major research objectives are:

1. Building a series of Rod-Plane models with different rod diameters and gap

distances in Coulomb. Coulomb is powerful 3D electric field design and analysis software. It can be used to build models (such as transformer, insulator and cables) and calculate their electric field as well as voltage distribution. Analyzing their electric field distributions with Boundary Element Method (BEM) and summarize differences and similarities.

2. Setting up a testing system to detect discharge signals in Rod-Plane Model. Comparing it with conventional PD detector to make sure that the detected signal is the discharge signal.
3. Recording discharge signals in Rod-Plane models and applying Pulse Sequence Analysis method (which concerns the cumulative effects of PDs) to analyze those signals. Comparing results of different models and investigating possible patterns which can be used to categorize discharge signals.
4. Building a model of a 15 kV cable with and without defects in Coulomb and determining the electric field distributions from core conductor to outer tube.
5. Testing PDs in a 15 kV bad-splice cable with a traditional PD detector to verify the existence of PDs in the cable and evaluating PD levels among different voltages.
6. Building a new testing system with FGB-based PD sensor. Testing the performance of this system with two sensors, one with resonant frequency of 42.7 kHz and the other 300 kHz.

1.3 Organization and Content

This thesis consists of six chapters. Chapter 1 presents an overview of background and research objectives. Chapter 2 provides the literature review, especially a review of

discharges, including an introduction of detection and analysis methods. Chapter 3 presents the Pulse Sequence Analysis method, its application to the analysis of PD signals and significant distribution patterns that this study found. Chapter 4 discusses the pre-test of bad-splice cable, including simulation model and test evaluation for PDs in different voltage levels. Chapter 5 describes the test system with FBG-based PD sensor and discusses test results from the experiment. Finally, Chapter 6 provides conclusions of the research and proposes future work.

Chapter 2

LITERATURE REVIEW ON DISCHARGES

2.1 Detection Methods

2.1.1 Electrical Methods

The direct result of PD is charge moving between electrodes. It will generate a small current and change the voltage between electrodes. The discharge duration is about 10 ns; thus it can be considered as a short pulse.

1. Test with Coupling Capacitor

This conventional method has been widely studied and applied to the actual test [5]. This is also the standard for partial discharges measurement in IEC 60270. It detects the pulse current caused by the discharges changing in the circuit. In this method, it uses coupling capacitor (C_k) as the sensor. The bandwidth is always located at the low frequency range.

The advantage of the test system based on this method is that it has high sensitivity. However, the discharges need to be calibrated every time before testing to verify correctly measurement of specified PD magnitude. Another disadvantage is that external noise can have a big effect on it, especially on-site measurement.

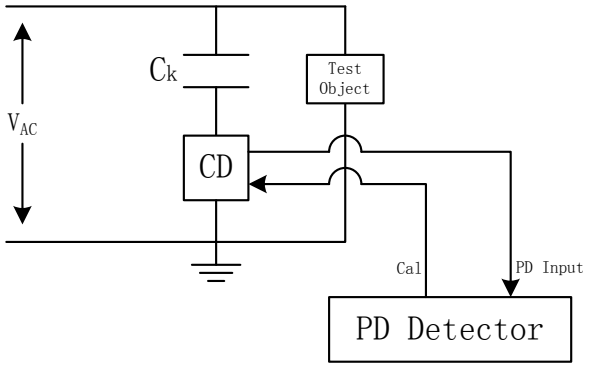

Figure 1 Conventional Test System

The schematic of the test system diagram is shown in Figure 1. CD is a coupling device which is used to pick up PD signals. This method was used to test many objects [6-9], including cables and switchgear.

2. Radio Influence Voltage Measurement

The basic circuit in this method is the same as in Figure 1, but it uses a Rogowski coil to act as the sensor to detect the pulse current. The strength of this method is that the bandwidth is higher than method mentioned before. Therefore, it can receive more information about PDs. Gaouda used this measurement to test PDs in transformers [6] and Cavallini applied it to polymeric cables [6, 10].

3. Ultra High Frequency Method

PDs are short pulses; thus they emit electromagnetic waves. The spectral characteristics of the electromagnetic wave are relative to the discharge source. The sensor used in ultra high frequency method is an antenna, such as a micro-strip antenna.

The detecting frequency level is high so that it can avoid the normal disturbance from corona and switch movement. Moreover, it can locate discharge sources and classify types of defects. However, the spread of electromagnetic waves is complicated as it is hard to pick up useful information from the antenna. Boggs and Stone utilized this method to study corona and partial discharges [11].

2.1.2 Non-electrical Methods

When PD happens, there are also other accompanying phenomena, such as sound, light and heat. These phenomena also involve characteristics of PDs [12].

1. Ultrasonic Method

There is ultrasonic wave associated with PDs. The common sensors are

microphone, hydrophone, accelerometer and acoustic emission sensor. Working bandwidth and sensitivity are two important indices for the ultrasonic method.

This method has a big advantage in locating the discharge sources. Compared to other methods, the ultrasonic method works better in complicated equipment. But the attenuation and distortion of the ultrasonic wave are the main problems. In actual measurement, it is always combined with electrical methods. This method has been used in transformers [13] and SF_6-insulated switchgear (GIS) [14].

2. Optical Fiber Method

The traditional optical method directly detects the light emitted by discharges [15]. The main limitation is that there is always no way to observe the light outside the insulation. Because of this, this method has not been applied to practical equipment. To overcome the problem, a method which combines ultrasonic with optical methods has been studied recently. The ultrasonic waves emitted by PD can create pressure on the optical fiber and change its transmission characteristics, such as refraction. The output light would be modulated by this fiber and can be read by demodulation. It has strong anti-jamming performance. There will be much less disturbance since the signal is light. Brian Culshaw did some research on this method [16] and Cosgrave applied it to gas insulated substation (GIS) [17].

3. Dissolved Gas Analysis Method

This is mainly utilized for transformers and SF6 equipment. The process of PD can lead to reaction of oil or SF6 and generate some kinds of gases. By detecting the composition and density of each kind of gases, the status of PD sources can be analyzed.

The advantage of dissolved gas analysis method is that it has a great performance

of anti-electromagnetic interference. However, the process of analysis takes a long time which means that it can predict the potential defects but cannot response to a sudden failure. Another drawback of Dissolved Gas Analysis is that it cannot be calibrated. In gas-insulated equipment [18] and transformers [19], this measurement has been used to analyze operational state of the equipment.

2.2 Analysis Methods

PD value in picocoulomb (pC) is widely used to evaluate PD situation. This is also the IEEE standard for partial discharge measurement. It is widely used and the technology is well developed. However, it only reflects the external performance of PD strength. The details of PDs are more important than pC values for PD evaluation [20]. To have a better understanding of PDs, distribution graphs, such as pulse height distribution (PHD) [21], phase resolved PD distribution (PRPD) [22, 23 and 24] and voltage resolved PD distribution (VRPD) [25], are utilized. However, these kinds of graphs still cannot show the internal characteristics of PDs. In addition, they are all based on pC value in which calibration is necessary. Besides, these distribution patterns are not the same among different detection systems for the same kind of discharges. This makes it difficult to make comparison and unified analysis.

Chapter 3

DISCHARGE STUDY WITH CONVENTIONAL METHOD

3.1 Introduction

A good understanding of discharge characteristics is necessary for further study of new analysis methods. This chapter is dedicated to examine corona discharges in rod-plane model. Corona discharge is an electrical discharge caused by the ionization of medium around the conductor surface when the strength of the electric field is high enough. The experiment uses the conventional method to detect the discharge values in pC. Three factors (rod diameter, gap distance and voltage level) have been explored to find their influence on discharge values.

3.2 Methods of Data Analysis

3.2.1 The Analysis of Variance

The analysis of variance (ANOVA) is a statistical model used to test differences between two or more means by analyzing variance [26]. Therefore, it can be used to test whether those three factors have influences on discharge values. For a model with three factors, the regression model can be simplified as:

$$y = \beta_0 + \beta_1 x_1 + \beta_2 x_2 + \beta_3 x_3 + \beta_{12} x_{12} + \beta_{23} x_{23} + \beta_{13} x_{13} + \beta_{123} x_{123} + \epsilon \quad (1)$$

in which, y is the discharge value; $x's$ are variables; $\beta's$ are regression coefficients; ϵ is error.

Assuming that factor 1 has a levels, factor 2 has b levels and factor 3 has c levels, the total sum of squares is,

$$SS_T = \sum_{i=1}^{a} \sum_{j=i}^{b} \sum_{k=1}^{c} (y_{ijk} - \bar{y}_{...})^2 \quad (2)$$

The sum of squares due to treatments for factor 3 is:

$$SS_{treatment} = c\sum_{i=1}^{a}\sum_{j=1}^{b}(\bar{y}_{ij.} - \bar{y}_{...})^2 \quad (3)$$

Then, the sum of squares due to error is:

$$SS_E = SS_T - SS_{treatment} \quad (4)$$

Mean squares due to treatment and error are:

$$MS_{treatment} = \frac{SS_{treatment}}{a-1} \quad (for\ factor\ 1) \quad (5)$$

$$MS_E = \frac{SS_E}{degree\ of\ freedom\ of\ error} \quad (6)$$

Therefore, the ratio is:

$$F_0 = \frac{MS_{treatment}}{MS_E} \quad (7)$$

The table of percentage points of the F distribution can be used to find the probability for F_0. This probability can reflect the effect of factors on results.

3.2.2 Time-Frequency Map

Time and frequency are two important characteristics for a signal. In this research, the signal that needs to be analyzed is pulse signal which should not be handled with Fourier analysis. Moreover, Fourier analysis has some limitations. Its characterization is either in time or frequency domains, which means that it cannot show the relationship between time and frequency. In this situation, time-frequency analysis (TF analysis) is the best choice [27, 28]. It can show both time and frequency characteristics of the signal at the same time.

In this experiment, Wigner-Ville distribution, a common method to analyze signal which shows the signal energy distribution in both time and frequency domains is used. For signal $s(t)$, its Wigner-Ville distribution is defined as:

$$W_z(t,f) = \int_{-\infty}^{+\infty} z\left(t+\frac{\tau}{2}\right) * z\left(t-\frac{\tau}{2}\right) * e^{-j2\pi\tau f} d\tau \quad (8)$$

in which, $z(t)$ is the expression in z domain.

To distinguish different PD signals, characteristics which can fully reflect the signal need to be found. In this experiment, five characteristics shown below have been used:

1. Time Gravity

   Assume the time domain expression of the signal is $S(t)$. Time gravity is defined as follow:

$$\bar{t} = \int t|S(t)|^2 dt \tag{9}$$

   Its standard deviation is formulated below:

$$\sigma_t^2 = \int (t - \bar{t})^2 |S(t)|^2 dt \tag{10}$$

   In this experiment, the first step is signal standardization which is postulated in the following formula:

$$S_N(t) = S(t) / \sqrt{\int_0^T S(\tau)^2 d\tau} \tag{11}$$

   The result of the time gravity will be:

$$\overline{t_N} = \int_0^T \tau S_N(\tau)^2 d\tau \tag{12}$$

2. Equivalent Time

   Equivalent time, which means the effective range of time around the time gravity, is defined below:

$$T = \sqrt{\int_0^T (\tau - \bar{t})^2 S_n(\tau)^2 d\tau} \tag{13}$$

3. Frequency Gravity

   Get $S(\omega)$ by Fourier transform of $S(t)$. Its standardization is:

$$S_N(\omega) = S(\omega) / \sqrt{\int_0^\infty |S(\omega)|^2 d\omega} \tag{14}$$

Then, the frequency gravity, also known as the center frequency, will be:

$$\overline{\omega_N} = \int_0^\infty \omega |S_N(\omega)|^2 d\omega \tag{15}$$

4. Equivalent Bandwidth

The equivalent bandwidth, which is defined as the effective range of bandwidth around the frequency gravity, is formulated in the following equation:

$$F = \sqrt{\int_0^\infty (\omega - \overline{\omega_N})^2 |S_N(\omega)|^2 d\omega} \tag{16}$$

Finally, time-frequency map (TF map) can be created with T and F, in which the same class of pulses would cluster together.

3.3 Experiment System

3.3.1 System Diagram

The diagram of the experiment system is shown in Figure 2.

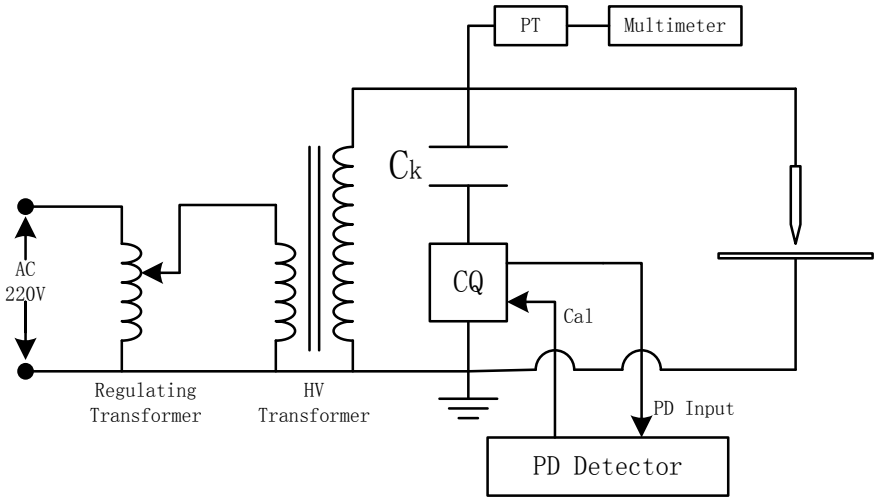

Figure 2 System Diagram

The high voltage is controlled by a regulating transformer, supplied by a 220 V power source. The 500 pF C_k is in series with the coupling quadripole (CQ), used to

detect the PD signal. A potential transformer (PT, with turns ratio 40250:67.08) is connected to the output of HV transformer and the voltage is read by a multimeter.

3.3.2 Calibration

The calibration is done with the internal calibrator of the PD Detector via the CQ. The CQ circuit is shown in Figure 3 below.

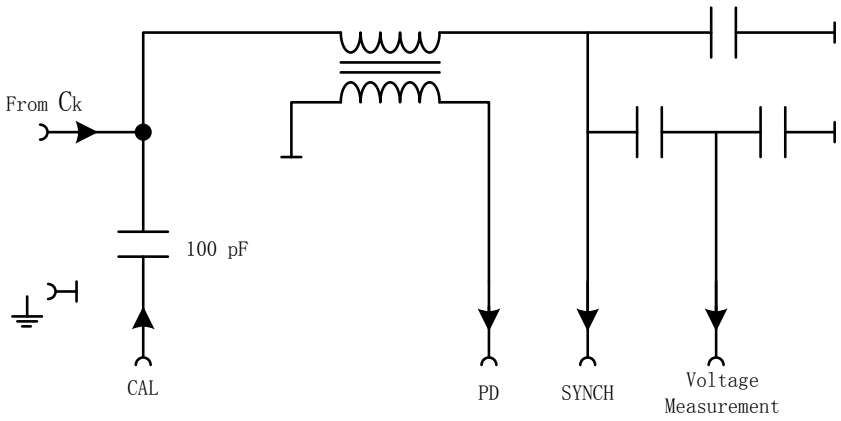

Figure 3 Coupling Quadripole

The calibration pulse coming from the PD detector is injected into the 100 pF capacitor at CAL port. The calibration signal can be detected by the PD Detector through the PD port. The calibration is done as per the PD Detector manual. All pC values of the internal calibrator (1 pC to 200 pC) have been checked for compliance with the selected values and the displayed pC values are found to be within the tolerances.

3.4 ANOVA Analysis

For the rod-plane model, there are three factors that may have an influence on PD behavior; these factors are rod diameter, gap distance and voltage level. Therefore, tests are conducted to see the trend when changing one factor with the other two fixed. The levels of three factors tested in this experiment are shown in Table 1. It can be seen that the total number of tests conducted in one repetition is 320 ($4\ D \times 4\ G \times 20\ V$).

Table 1 Levels of Three Factors

Rod Diameter (D) /mm	0.91, 1.58, 1.96, 2.36
Gap Distance (G) /mm	22, 20, 18, 16
Voltage Level (V) /kV	1kV to 20kV, with 1kV step

3.4.1 Relation between PD value and Voltage

In this experiment, rod diameter was fixed to a certain value. PD values were recorded with the increasing of voltage levels. It was repeated two times to guarantee the accuracy of the results. The results are shown below.

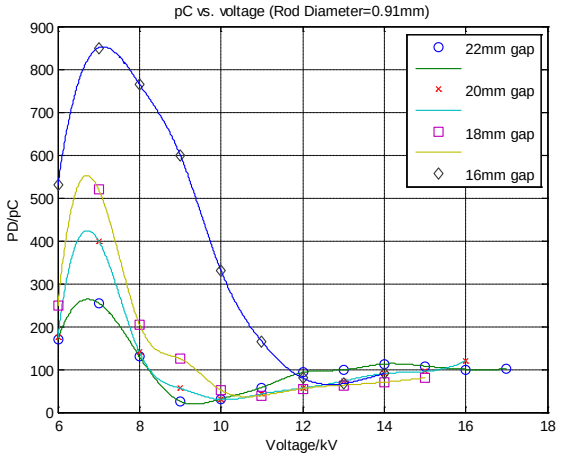

Figure 4 pC /V when D=0.91 mm

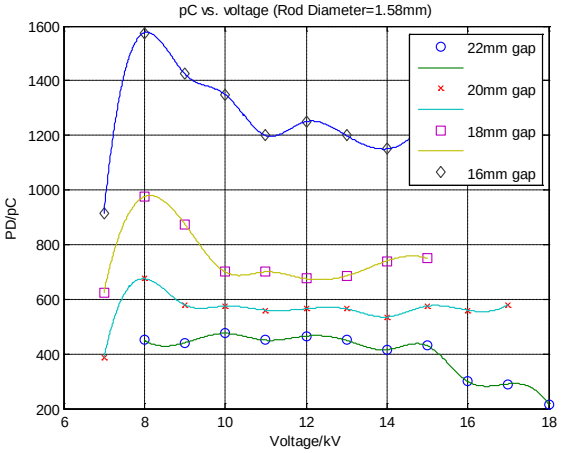

Figure 5 pC /V when D=1.58 mm

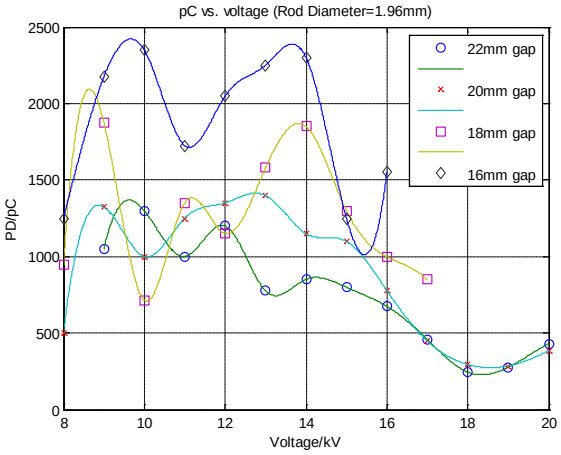

Figure 6 pC /V when D=01.96 mm

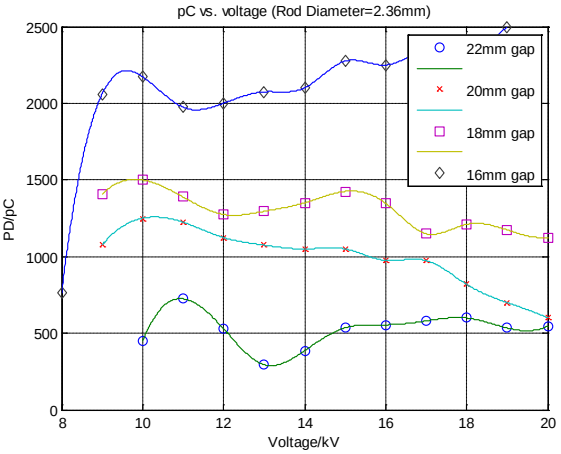

Figure 7 pC /V when D=2.36 mm

3.4.2 Relation between PD value and Rod Diameter

In this experiment, gap distance was fixed to a certain value. PD values were recorded with the changing of rod diameters. It was repeated two times to guarantee the

accuracy of the results. The results are shown below.

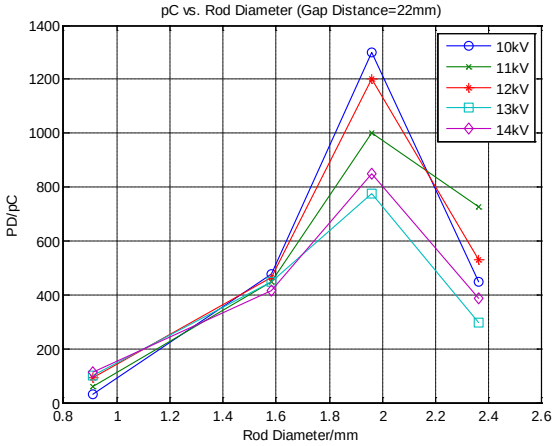

Figure 8 pC /D when G=22 mm

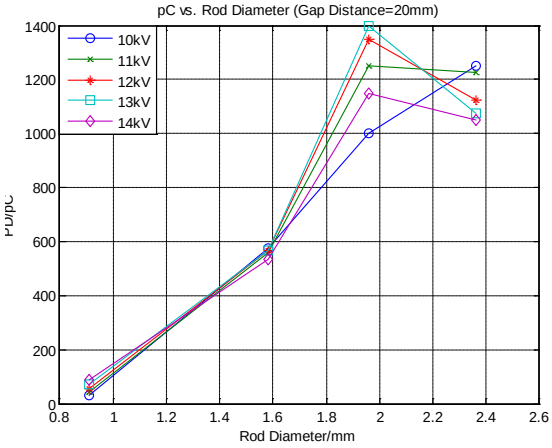

Figure 9 pC /D when G=20 mm

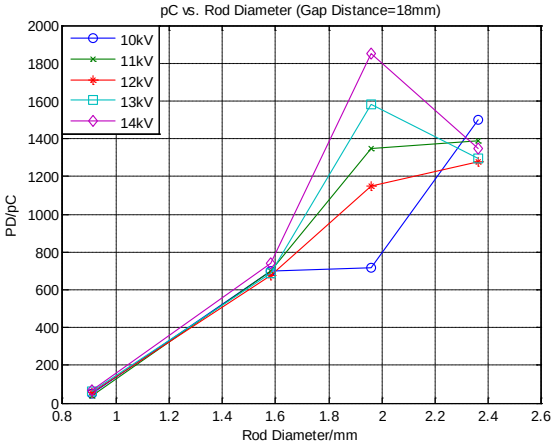

Figure 10 pC /D when G=18 mm

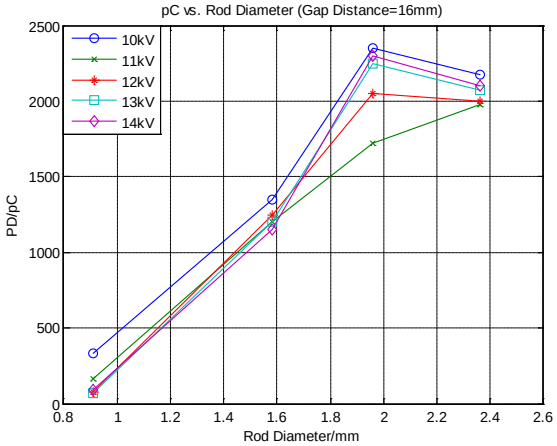

Figure 11 pC /D when G=16 mm

3.4.3 Relation between PD value and Gap Distance

In this experiment, voltage level was fixed to a certain value. PD values were recorded with the changing of gap distances. It was repeated two times to guarantee the accuracy of the results. The results are shown in next page.

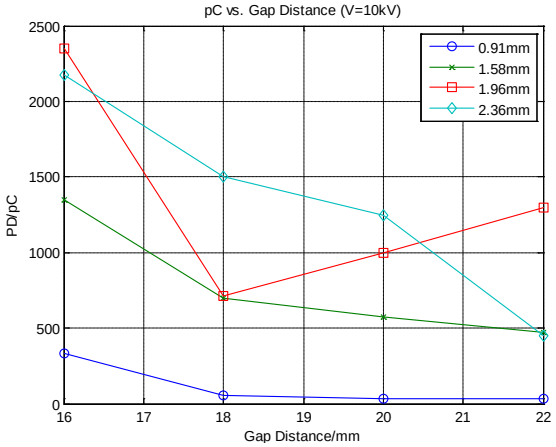

Figure 12 pC /G when V=10 kV

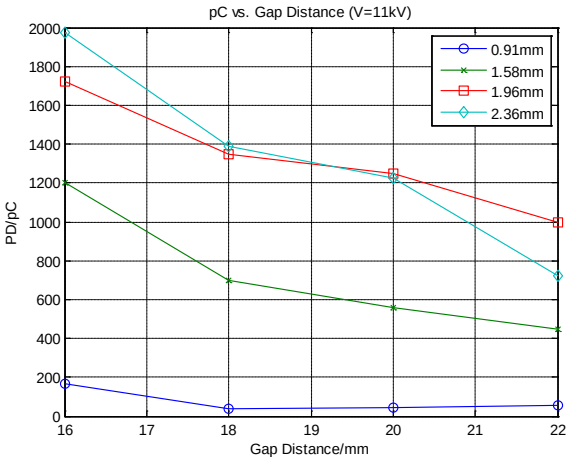

Figure 13 pC /G when V=11 kV

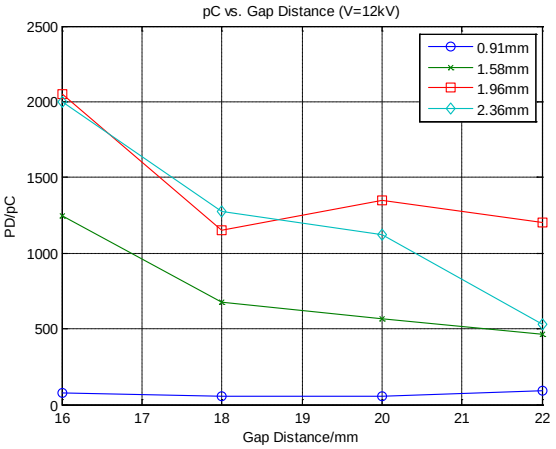

Figure 14 pC /G when V=12 kV

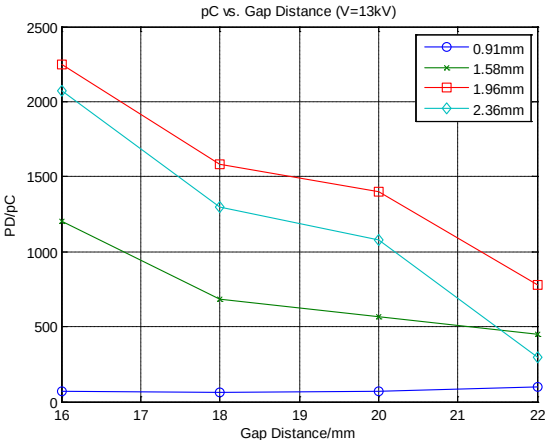

Figure 15 pC /G when V=13 kV

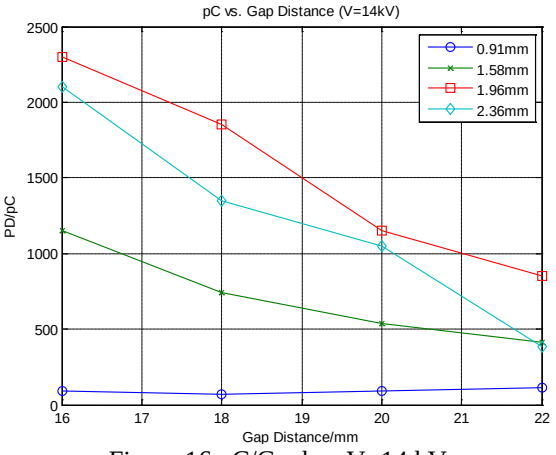

Figure 16 pC/G when V=14 kV

3.4.4 Analysis of Data

The data to analyze the effects of D, G and V are taken from voltage level between 10 kV and 14 kV. ANOVA table for PD value is shown in Table 2.

Table 2 ANOVA Table for PD Value

	Degrees of Freedom	Sum of Squares	Mean Square	F_0	Prob>F_0
Rod Diameter (R)	3	44074316	14691438.67	199.95	<0.0001
Gap Distance (G)	3	16817548	5605849.33	76.30	<0.0001
Voltage Level (V)	4	19477	4869.25	0.07	0.9918
RG	9	6771265	752362.78	10.24	<0.0001
RV	12	439529	36627.42	0.50	0.91
GV	12	901948	75162.33	1.02	0.44
RGV	36	1816685	50463.47	0.69	0.89
Error	80	5878026	73475.33	/	/
Total	159	76718794	/	/	/

3.5 Time-Frequency Analysis

By observing the pulse signal waveform, the duration is around 2 ns. To make sure that the pulse signal can be reverted successfully, the sample rate is 200 Mpts/s. 100 ms data was recorded each time and this process was repeated 10 times for each situation to guarantee the accuracy of the result.

3.5.1 Differences among Rod Diameters

Voltage level was fixed to be 13.2 kV and gap distance 18 mm. Four levels of rod diameters (2.98 mm, 2.36 mm, 1.96 mm and 1.58 mm) have been chosen. Time-frequency maps are shown in next page.

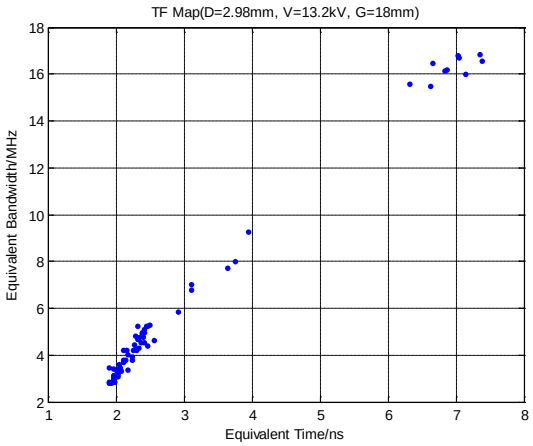

Figure 17 TF Map for D=2.98 mm

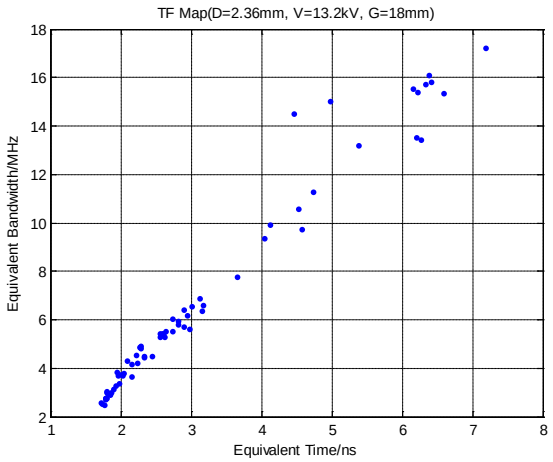

Figure 18 TF Map for D=2.36 mm

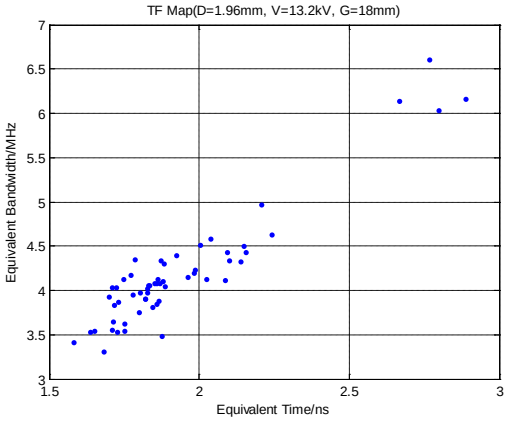

Figure 19 TF Map for D=1.96 mm

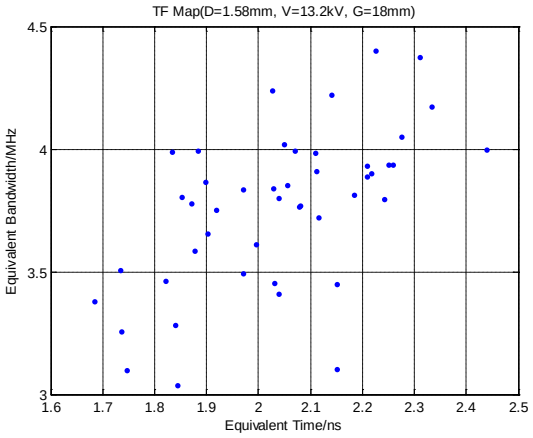

Figure 20 TF Map for D=1.58 mm

3.5.2 Differences among Gap Distances

Voltage level was fixed to be 13.2 kV and rod diameter 2.36 mm. Four levels of gap distances (22 mm, 20 mm, 18 mm and 16 mm) have been chosen. Time-frequency maps are shown in next page.

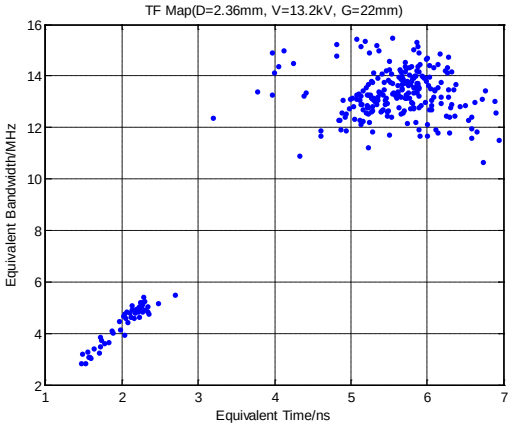

Figure 21 TF Map for G=22 mm

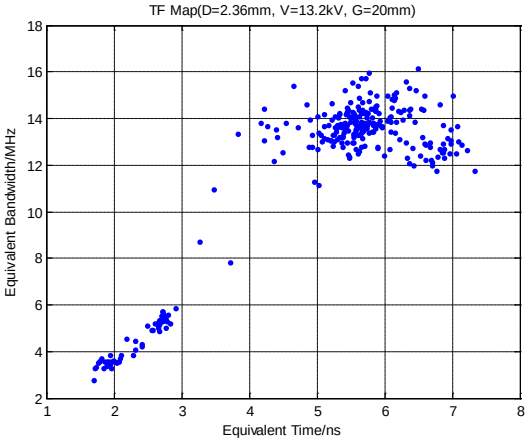

Figure 22 TF Map for G=20 mm

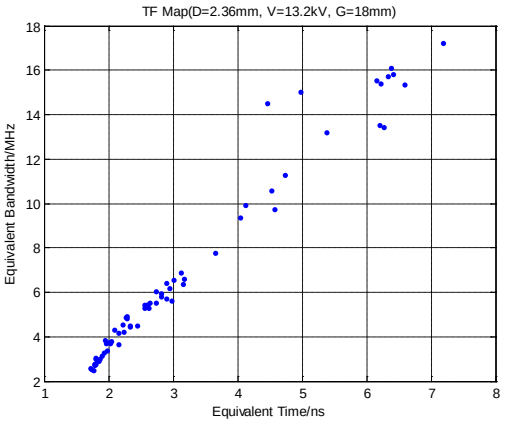

Figure 23 TF Map for G=18 mm

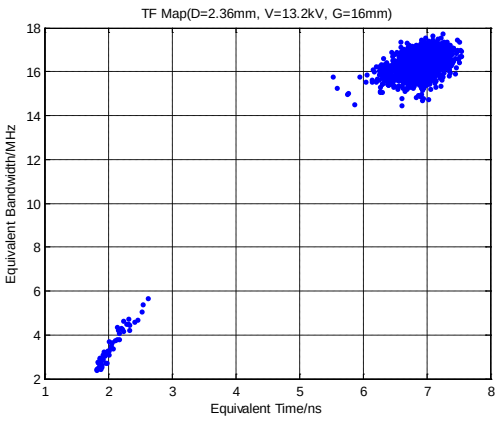

Figure 24 TF Map for G=16 mm

3.5.3 Differences among Voltages

Gap distance was fixed to be 18 mm and rod diameter 2.36 mm. Four levels of voltages (14.4 kV, 13.2 kV, 12 kV and 10.8 kV) have been chosen. Time-frequency maps are shown in next page.

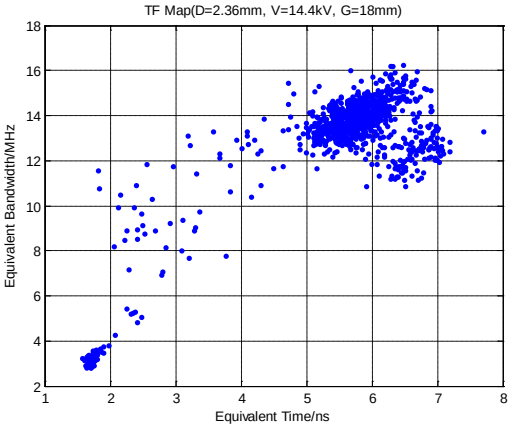

Figure 25 TF Map for V=14.4 kV

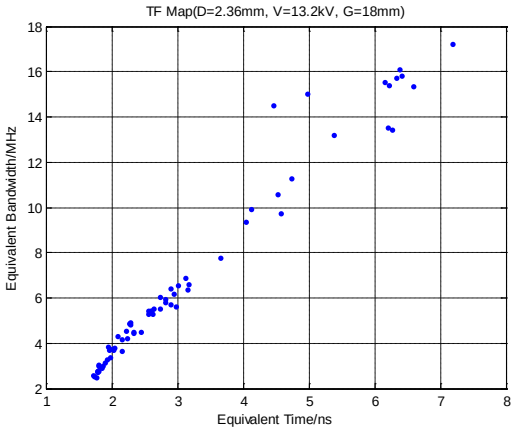

Figure 26 TF Map for V=13.2 kV

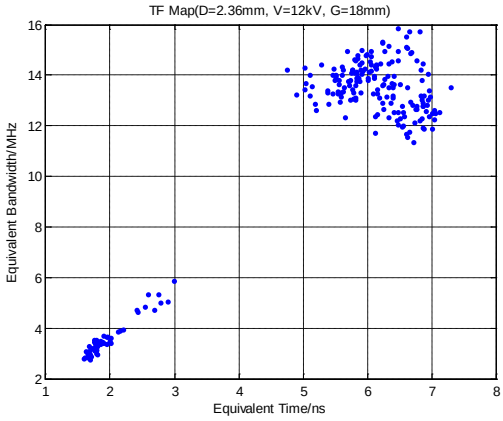

Figure 27 TF Map for V=12 kV

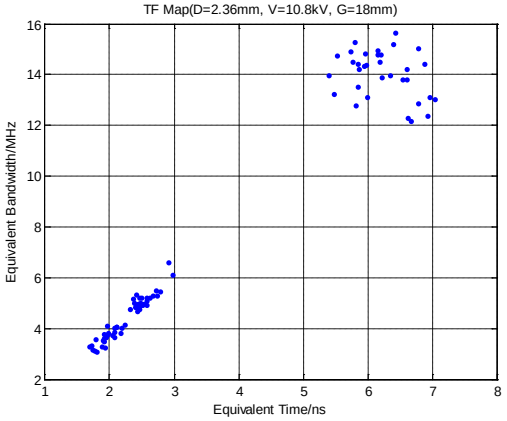

Figure 28 TF Map for V=10.8 kV

3.5.4 Differences among Different Types of Discharges

Three types of discharges, namely corona discharge in Rod-Plane Model (D=2.36 mm, V=13.2 kV and G=20 mm), PD in cable (V=30 kV) and PD in Rod-Rod model in epoxy (V=12 kV), were analyzed. Time-frequency maps are shown in next page.

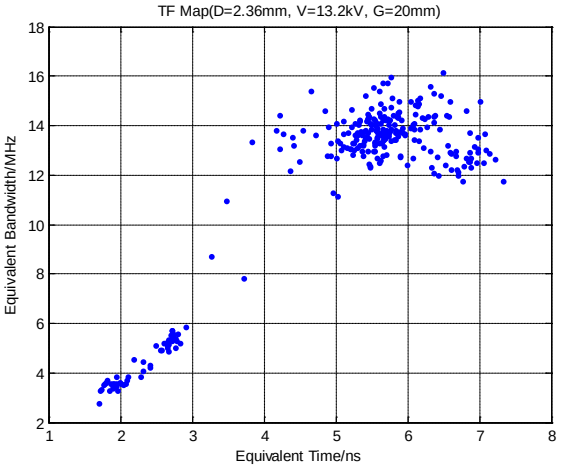

Figure 29 TF Map for Rod-Plane Model

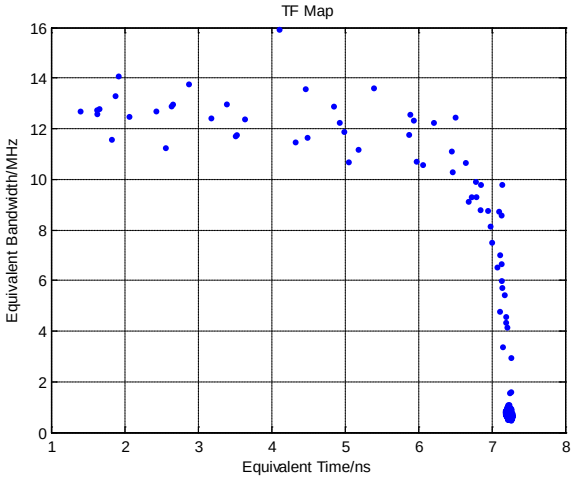

Figure 30 TF Map for Cable

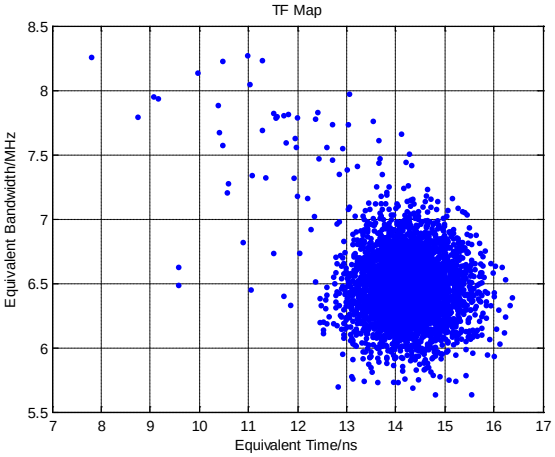

Figure 31 TF Map for Rod-Rod Model in Epoxy

3.6 Discussion

For corona discharge value:

1. Using 99.99% confidence level, rod diameter and gap distance have effects on corona discharge value.
2. Voltage level does not have any effect on corona discharge value.
3. The discharge value will increase with the increase of rod diameter or the decrease of gap distance.

By detecting discharge values with conventional method, it can be concluded that the main factors that can affect PDs are rod diameter and gap distance.

For Time-frequency map:

1. It can be seen that the change of factors in Rod-Plane Model can affect the PD pulse. The equivalent time and bandwidth are not unique. Their distribution can change with different combination of factors. However, they are more likely random with no tendency.
2. There are significant differences among types of discharges. Each type of discharges has a unique distribution pattern.

Time-frequency map cannot show the tendency for the parameters' changing in rod-plane model. However, it can be used to classify different kinds of discharges. However, there is a key limitation. Different test systems generate different time-frequency distributions, which mean that they have different classification database [16]. In such situation, even for the same types of discharge in the same insulation, the time-frequency map would be different when different systems are used to test the sample. This will increase the degree of difficulty for further analysis.

Chapter 4

STUDY OF ROD-PLANE MODEL WITH PULSE SEQUENCE ANALYSIS METHOD

4.1 Introduction

For conventional PD detection systems, output signals are generated by the coupling capacitor. The PD values and frequency information are affected by C_k, capacitor of test object and system circuit. This is also the reason why calibration is necessary. In this situation, different detection systems will have different PD patterns databases for each test object, which makes it hard to do a unified analysis and compare PDs in different equipment.

Pulse Sequence Analysis method is discussed in this chapter. It focuses on the relation between two adjacent discharges, which means it is not necessary to do the calibration. Rod-Plane Models are utilized to test the performance of the Pulse Sequence Analysis method. Meanwhile, the characteristics among different gap distances and rod diameters are studied, as well as different types of discharges.

4.2 Experiment Theory

4.2.1 Pulse Sequence Analysis Method

Conventional PD analysis methods can detect PD signals with high sensitivity, but they cannot reflect the real physical phenomena properly. In an actual situation, space charge remaining near the defect inside the insulation from one PD can affect the following PD by changing its ignition conditions. This is even more important during the early stage of insulation aging when the discharge path is forming [29, 30]. Conventional PD analysis methods consider each PD as an independent event and ignore this important aspect.

However, one advantage of the pulse sequence analysis method is that it considers the connection between consecutive discharges. The local electric fields and their changes are the main factors that affect the occurrence of PDs, especially consecutive PDs. The most significant external performance of them is the change in supply voltage between two neighboring discharges [31]. Both voltage and phase changes of supply voltage are studied and their definitions are shown in Figure 32. Another advantage is that calibration is not necessary. Since only voltage and phase positions are concerned, they have no connection with the pC values of PD signals, which need calibration. As a result, even tested by different detection systems, the results can be consistent [32].

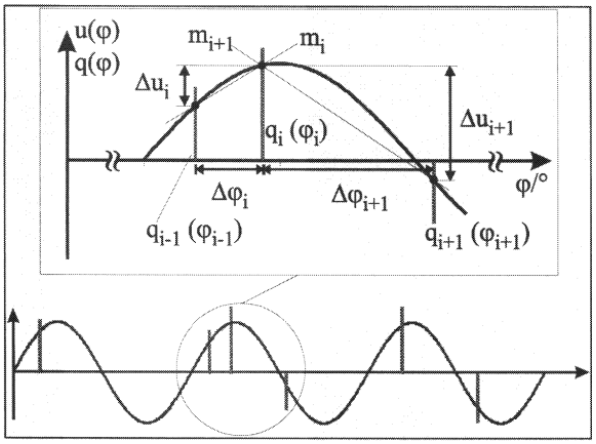

Figure 32 Definition of Voltage and Phase Changes [32]

4.2.2 Simulation of Rod-Plane Model

Two series of models have been built in Coulomb. One is changing gap distance with a constant rod diameter and the other is changing rod diameter with a constant gap distance.

Taking 18 mm gap distance and 0.91 mm rod diameter as sample, the model is shown in Figure 33.

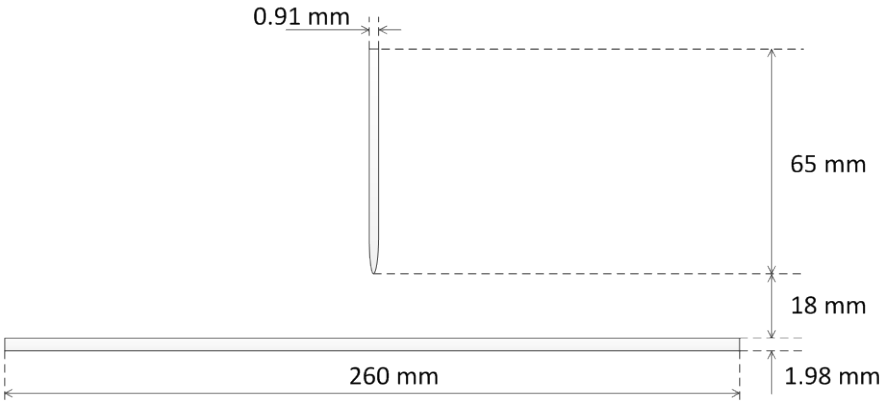

Figure 33 Simulation Model

All simulation results are combined and plotted in one figure with Matlab. The outputs are shown in Figure 34 and 35.

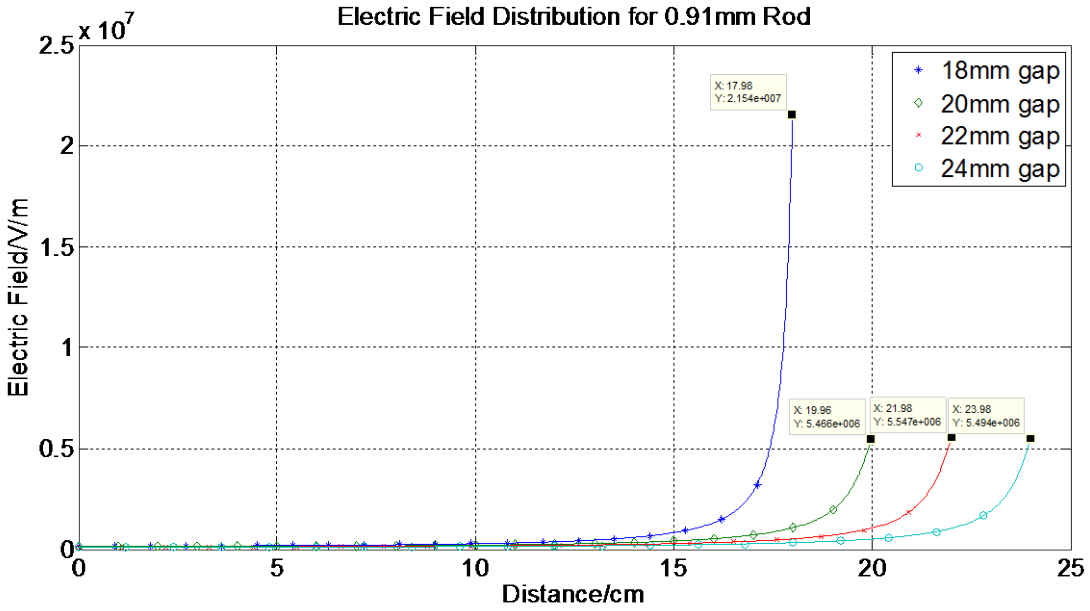

Figure 34 Electric Field Distribution for 0.91 mm Rod Diameter

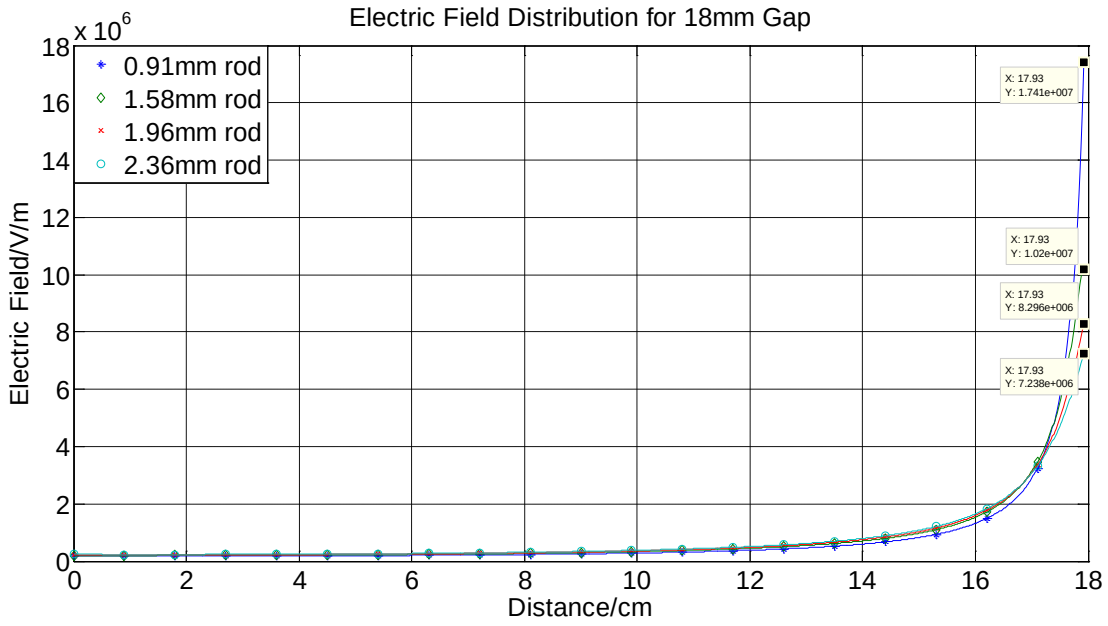

Figure 35 Electric Field Distribution for 18 mm Gap Distance

In Figure 34 and 35, the x-axis is the path of the gap, from plane to rod. The electric field values at the point of the rod are shown in Table 3 and 4.

Table 3 Electric Field for 0.91 mm Rod Diameter

Rod Diameter/mm	0.91			
Gap Distances/mm	18	20	22	24
Electric Field/V/m	2.15×10^7	5.61×10^6	5.55×10^6	5.49×10^6

Table 4 Electric Field for 18 mm Gap Distance

Gap Distance/mm	18			
Rod Diameters/mm	0.91	1.58	1.96	2.36
Electric Field/V/m	1.74×10^7	1.02×10^7	8.30×10^6	7.24×10^6

It can be concluded that the electric field will increase with the increase of gap distances from Table 3 and decrease with the increase of rod diameters from Table 4.

4.3 System Setup

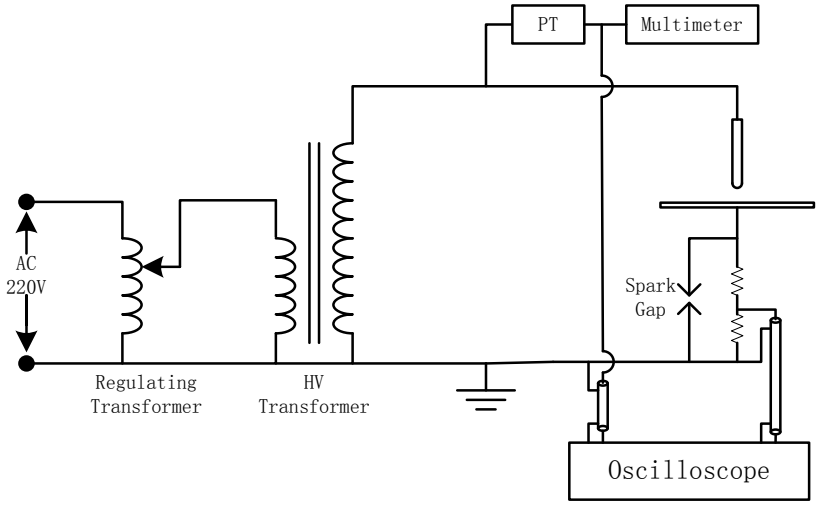

Figure 36 System Diagram

The PD signals are recorded by an oscilloscope with high sampling rate and long record length (LeCroy waverunner 104 MXi). Meantime, the supply voltage is also recorded after a potential transformer (PT, with turn ratio 40250:67.08) which is connected with the high voltage side of the system. The voltage level during the experiment is read by a multimeter. The PD signals are detected by a resistance. To limit the input voltage of oscilloscope, another divider resistance and a 75 V spark gap are utilized.

4.4 Tests and Results

To pinpoint the location of each PD signal, the sampling rate was set as 250 Mpts/s. The recording time was 200 ms, and it was repeated two times. Figure 37 shows PDs in one cycle. There are two clusters of PDs; one is around 270^{o} (named Type 1) and the other around 70^{o} (named Type 2). Type 1 happens around the negative peak value of supply voltage and has a high repetition. Type 2 happens before the peak value of supply

voltage and has a very low repetition. All tests were conducted at 15 kV. Four levels of rod diameter and gap distance were tested. Parameters are shown in Table 5.

Table 5 Parameters of Rod Diameters and Gap Distances

Rod Diameter (D) /mm	0.91, 1.58, 1.96, 2.36
Gap Distance (G) /mm	18, 20, 22, 24

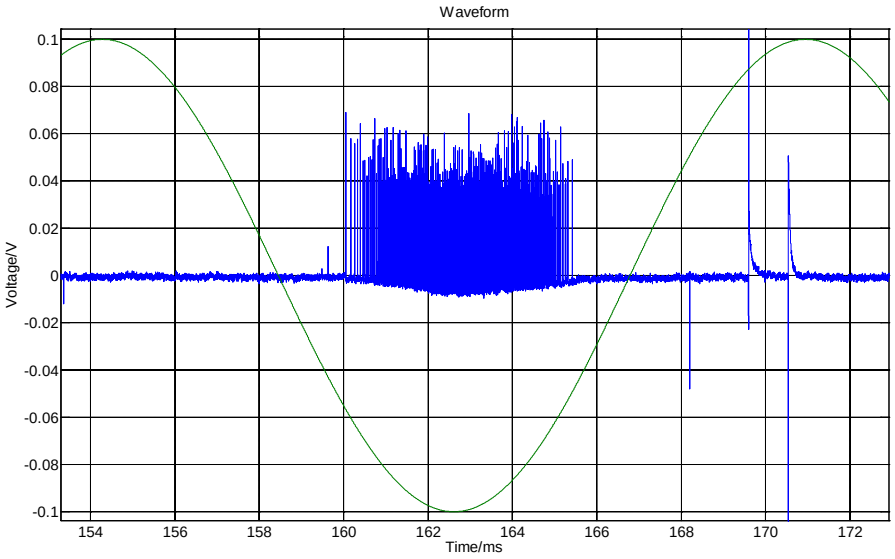

Figure 37 Two Types of PDs

4.4.1 $\Delta u/\Delta\varphi$ Graph

The following four figures show $\Delta u/\Delta\varphi$ graph for Type 1 PDs with 2.36 mm rod diameter.

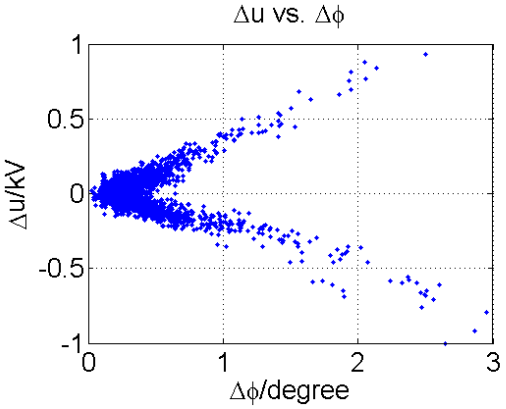

Figure 38 D=2.36mm and G=18 mm

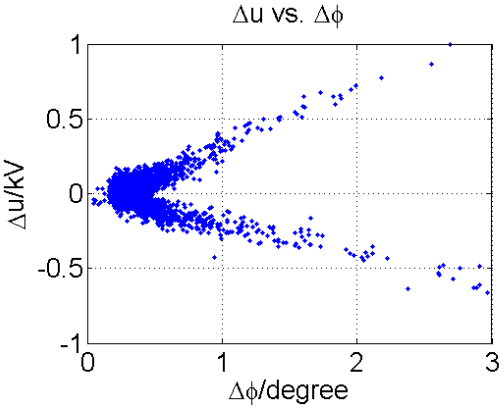

Figure 39 D=2.36 mm and G=20 mm

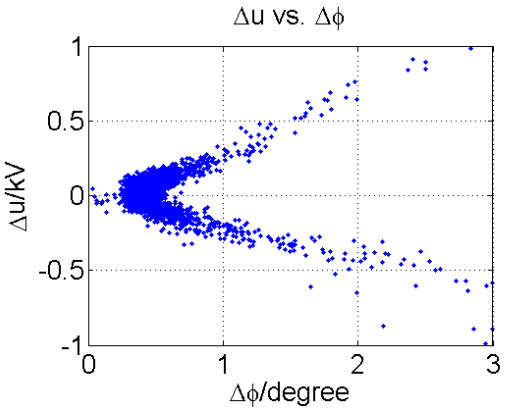

Figure 40 D=2.36 mm and G=22 mm

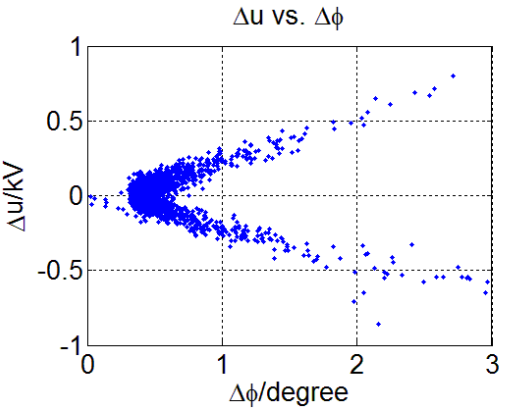

Figure 41 D=2.36 mm and G=24 mm

The following four figures show $\Delta u/\Delta\varphi$ graph for Type 1 PDs with 24 mm gap distance.

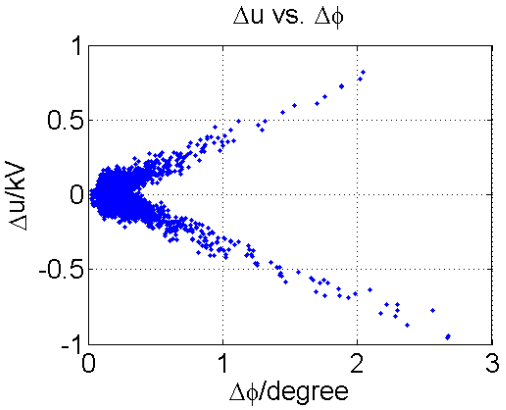

Figure 42 D=0.91 mm and G=24 mm

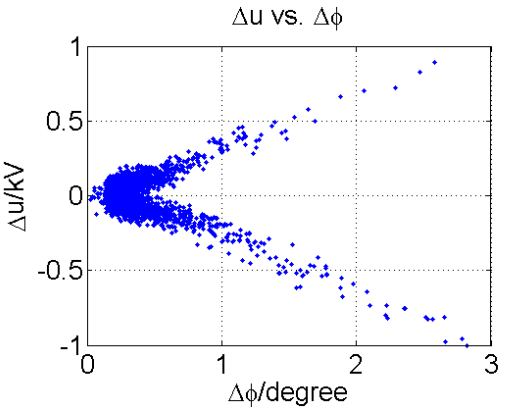

Figure 43 D=1.58 mm and G=24 mm

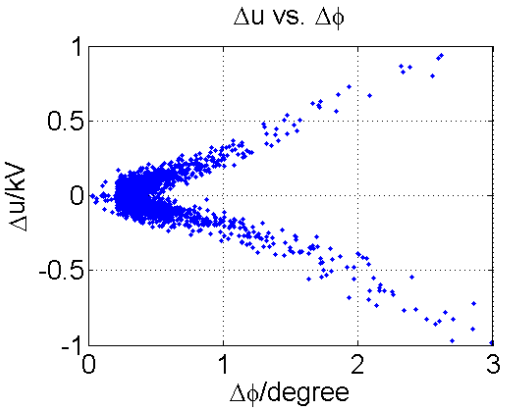

Figure 44 D=1.96 mm and G=24 mm

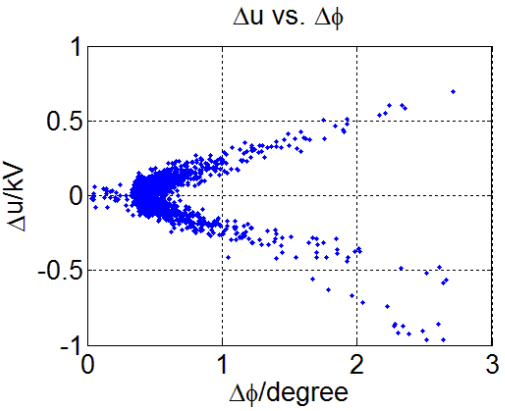

Figure 45 D=2.36 mm and G=24 mm

The following four figures show $\Delta u/\Delta\varphi$ graph for Type 2 PDs with 2.36 mm rod

diameter.

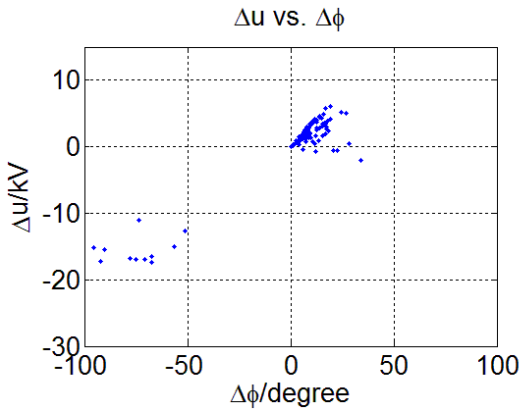

Figure 46 D=2.36 mm and G=18 mm

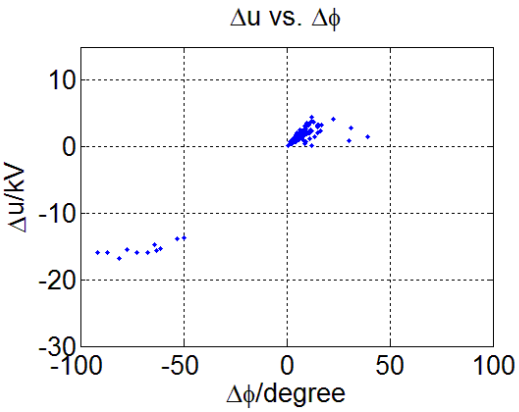

Figure 47 D=2.36 mm and G=20 mm

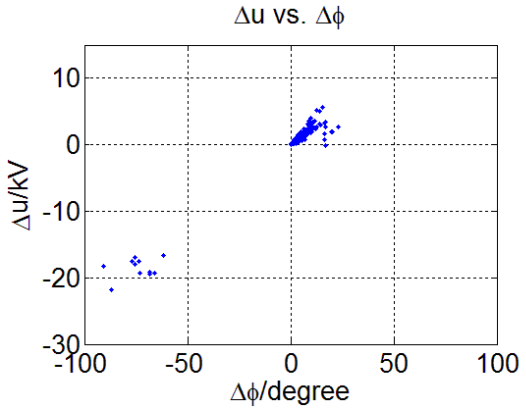

Figure 48 D=2.36 mm and G=22 mm

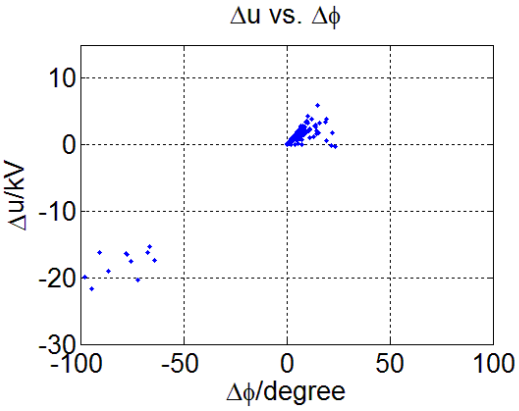

Figure 49 D=2.36 mm and G=24 mm

The following four figures show $\Delta u/\Delta\varphi$ graph for Type 2 PDs with 24 mm gap distance.

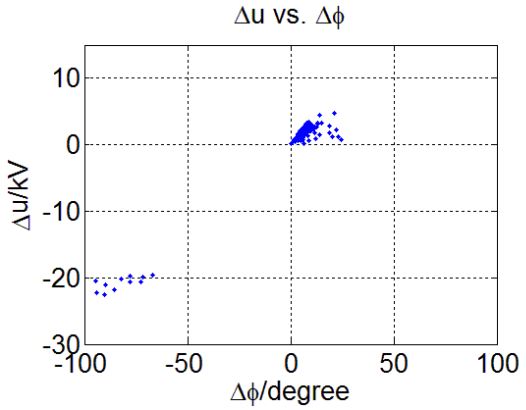

Figure 50 D=0.91 mm and G=24 mm

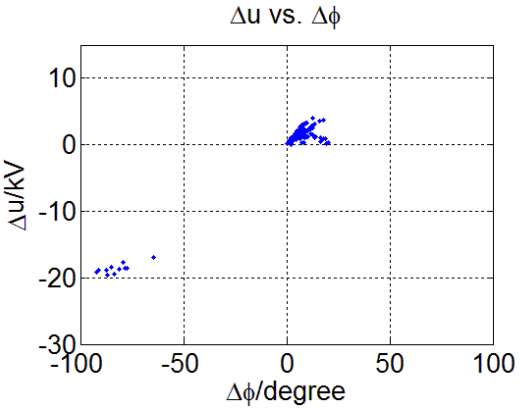

Figure 51 D=1.58 mm and G=24 mm

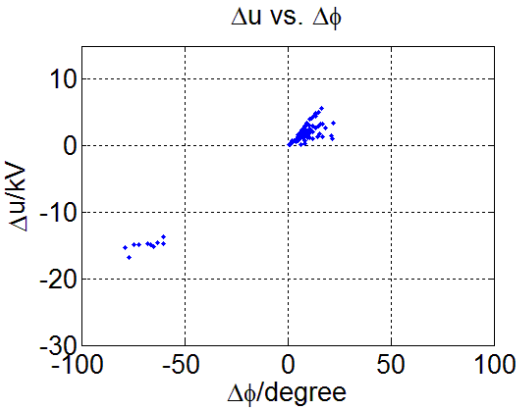

Figure 52 D=1.96 mm and G=24 mm

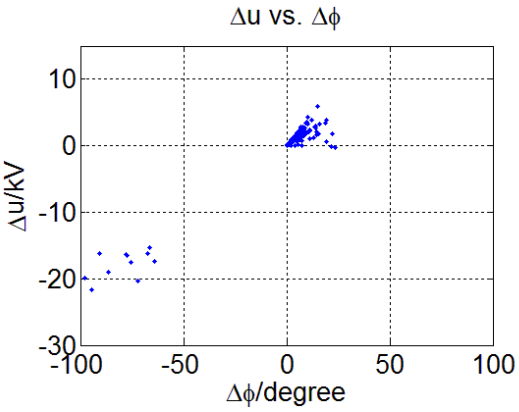

Figure 53 D=2.36 mm and G=24 mm

4.4.2 $\Delta u(i+1)/\Delta u(i)$ Graph

The following four figures show $\Delta u(i+1)/\Delta u(i)$ graph for Type 1 PDs with 2.36 mm rod diameter.

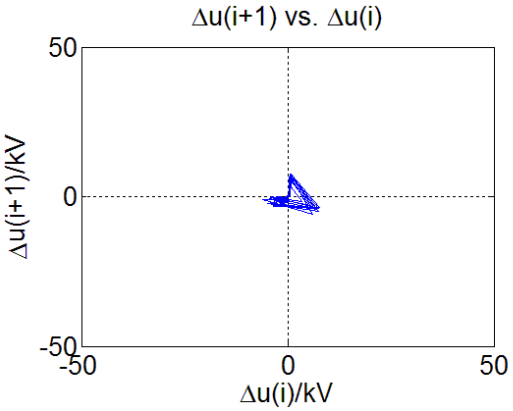

Figure 54 D=2.36 mm and G=18 mm

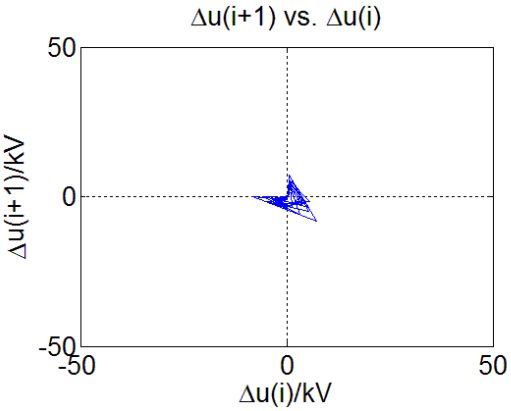

Figure 55 D=2.36 mm and G=20 mm

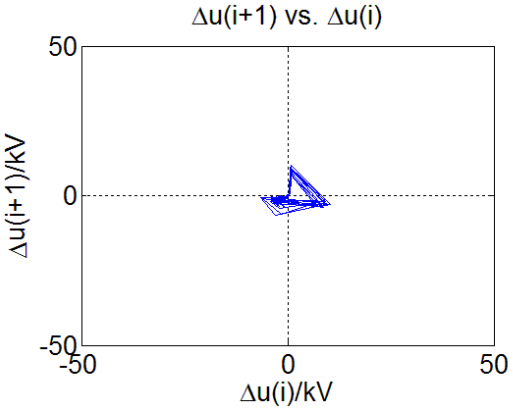

Figure 56 D=2.36 mm and G=22 mm

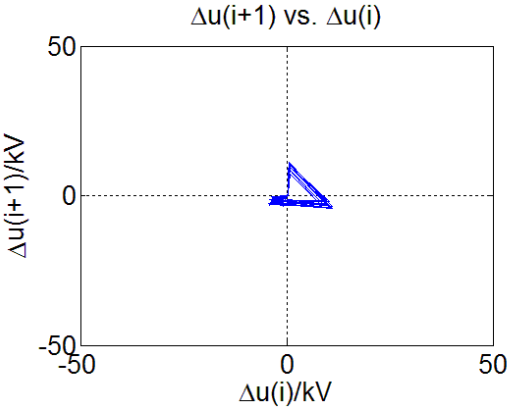

Figure 57 D=2.36 mm and G=24 mm

The following four figures show $\Delta u(i+1)/\Delta u(i)$ graph for Type 1 PDs with 24 mm gap distance.

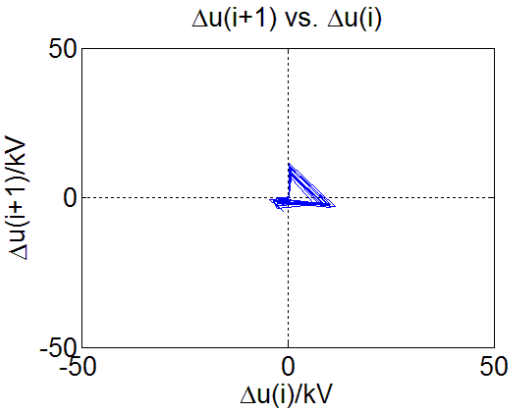

Figure 58 D=0.91 mm and G=24 mm

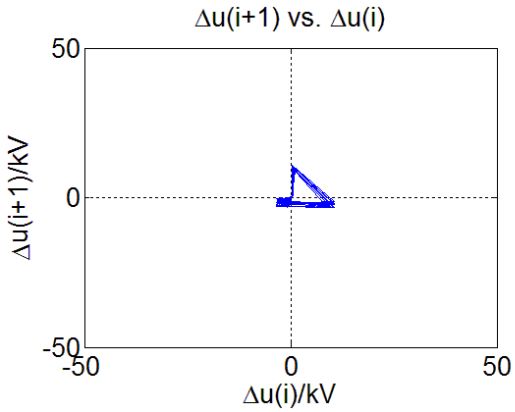

Figure 59 D=1.58 mm and G=24 mm

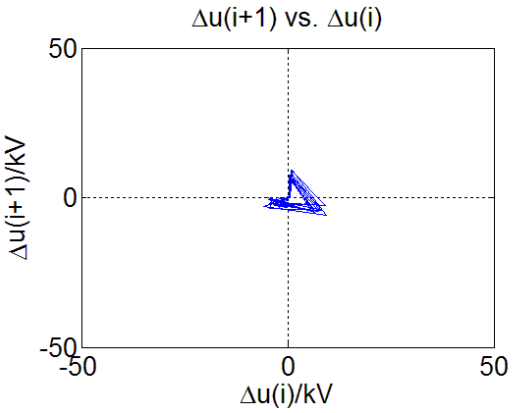

Figure 60 D=1.96 mm and G=24 mm

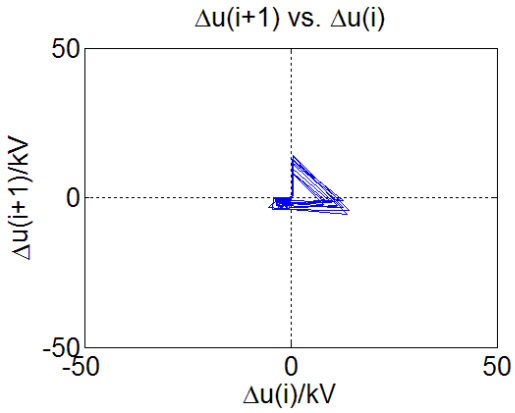

Figure 61 D=2.36 mm and G=24 mm

The following four figures show $\Delta u(i+1)/\Delta u(i)$ graph for Type 2 PDs with 2.36 mm rod diameter.

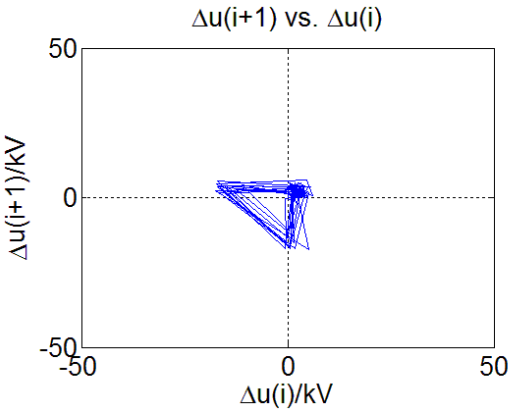

Figure 62 D=2.36 mm and G=18 mm

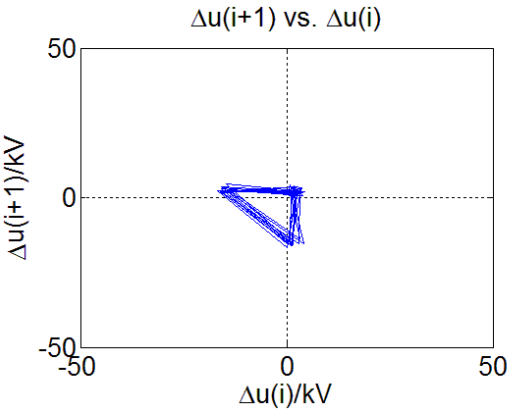

Figure 63 D=2.36 mm and G=20 mm

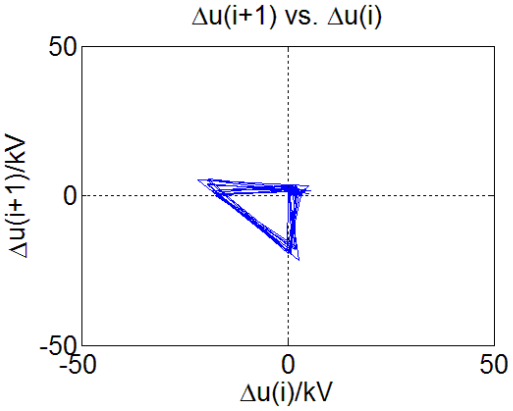

Figure 64 D=2.36 mm and G=22 mm

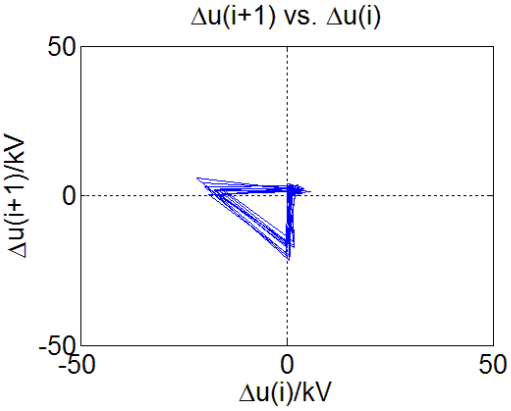

Figure 65 D=2.36 mm and G=24 mm

The following four figures show $\Delta u(i+1)/\Delta u(i)$ graph for Type 2 PDs with 24 mm gap distance.

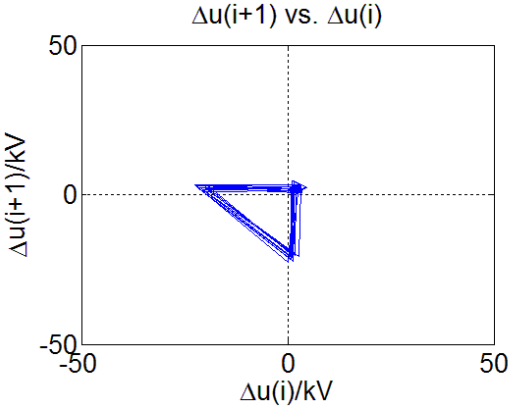

Figure 66 D=0.91 mm and G=24 mm

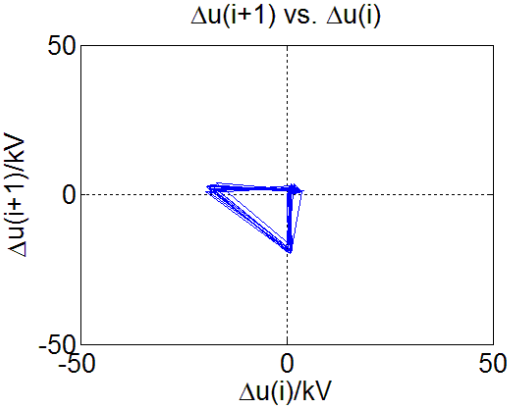

Figure 67 D=1.58 mm and G=24 mm

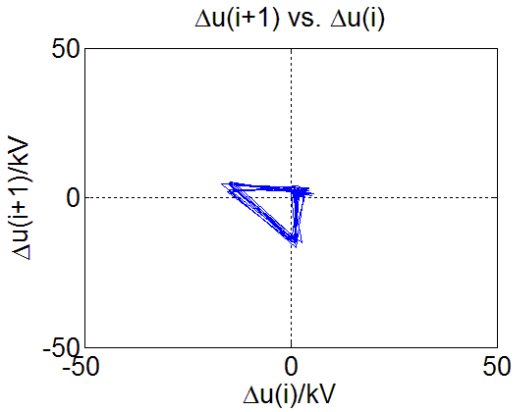

Figure 68 D=1.96 mm and G=24 mm

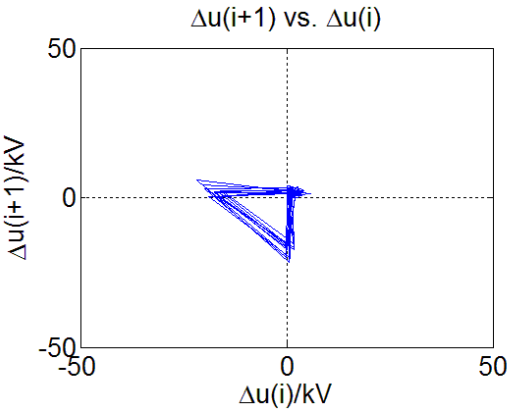

Figure 69 D=2.36 mm and G=24 m

4.4.3 Discussion

$\Delta u/\Delta\varphi$ pattern is used to show the relation between voltage difference and phase position difference for two adjacent discharges. And $\Delta u(i+1)/\Delta u(i)$ pattern is used to describe the connection between two contiguous voltage differences.

For either type of discharge, the distribution patterns in both $\Delta u/\Delta\varphi$ and $\Delta u(i+1)/\Delta u(i)$ figures exhibit a high degree of consistency among different rod diameters and gap distances. However, for the same kind of figures, $\Delta u/\Delta\varphi$ and $\Delta u(i+1)/\Delta u(i)$, the distribution patterns are completely different between two types of discharges. Meanwhile, this difference also exhibits a high degree of consistency.

For the same kind of discharge, the change of rod diameter and gap distance cannot affect the relation between two adjacent discharges and their distribution patterns are very stable. However, the relations between two adjacent discharges in different types of discharges are not the same. Therefore, both $\Delta u/\Delta\varphi$ and $\Delta u(i+1)/\Delta u(i)$ figures can be utilized to classify different types of discharges. Meantime, for the same kind of discharge, the distribution patterns have a high consistency.

Chapter 5

EXPERIMENT WITH FBG-BASED PD SENSOR

5.1 Introduction

The conventional detection methods used today are mainly based on electrical methods. However, there are many limitations. Electrical signals are easily disturbed by the environmental electric field noise, which can decrease the SNR and make it hard to detect useful signals. Moreover, the attenuation and disturbance along the signal transmission line also limit the distance between analysis equipment and detection sensor. As a result, remote monitoring and analysis become very difficult.

Compared with conventional detection systems, FBG-based PD sensor can turn electrical PD signals into wavelength signals at the sensor and transfer light signals instead of electrical signals. In this situation, there is almost no disturbance along the transmission. In this chapter, a 15 kV XLPE cable is utilized to explore the performance of the FBG-based PD sensor.

5.2 Experiment Theory

5.2.1 PDs in Cable

Compared with corona discharge, PD is a localized breakdown of dielectric inside the insulation. For a defective cable, PDs are generated within defects inside the cable. The locations of these defects can be diverse, such as part of semiconductor, in or between the insulation and inside wall of outer tube [33]. These defects may be induced by manufacture and penetration of impurities during service. As a result, there will be numbers of paths and different lengths of paths for PDs. Besides, since location and size of defects are diverse, PD signals are various for different defects [29].

5.2.2 FBG-based PD Sensor

Compared with the conventional method mentioned previously, FBG promises more advantages, such as compact size, low cost and immunity to electromagnetic interference [34, 35]. However, the signal reflected by an FBG sensor is typically low in power due to the spectral slicing process, thereby resulting in a limited dynamic range and decreased sensitivity. While it has been shown that the resolution of the wavelength-to-power mapping can be improved with FBGs having narrow bandwidth, this exacerbates the problem of power efficiency as even less power is reflected by the sensor [36]. Moreover, FBG-based sensor can be mounted to the device and other fiber optics sensors such as temperature, moisture and loading can be installed to help to correlate PD with these operational and environment condition.

5.2.3 Simulation of Cable

To better understand the electric field distribution in a defective cable, Coulomb is used to do the simulation.

An intact cable model is shown in the Figure 70.

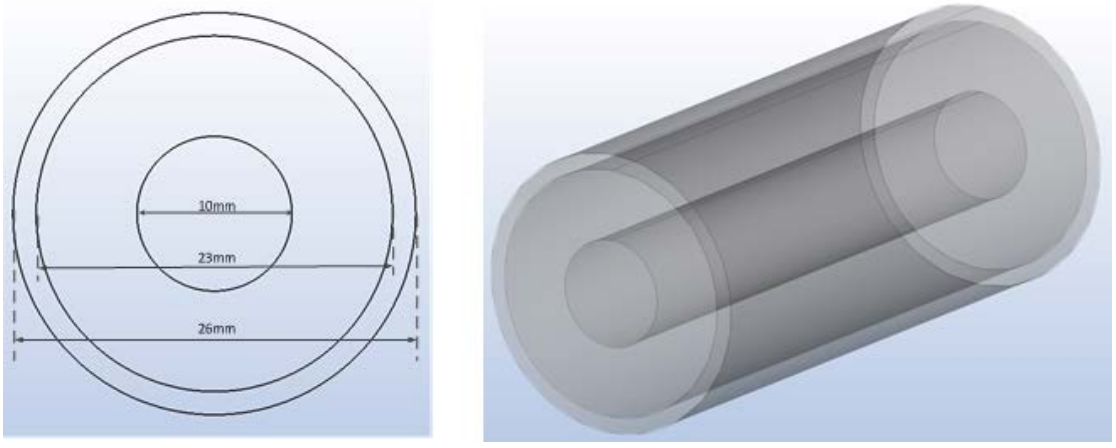

Figure 70 Intact Cable Model

The cable in Figure 70 is composed of a core conductor, a grounding cover and an

insulation medium. The core conductor is made of aluminum while the grounding cover is made of copper. The insulating medium is cross-linked polyethylene (XLP), with permittivity 2.3. The supplied voltage is the magnitude of 15 kV AC, which is 21.213 kV.

For the intact cable, the simulation result for the electric field is shown below.

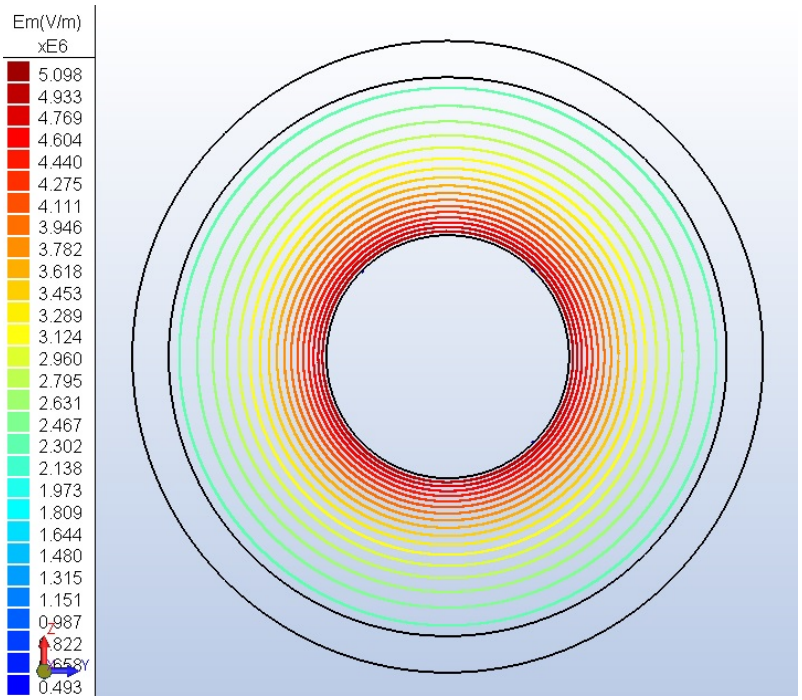

Figure 71 Electric Field of Intact Cable

The following model is set with a semicircle gap near the conductor core (shown in Figure 72).

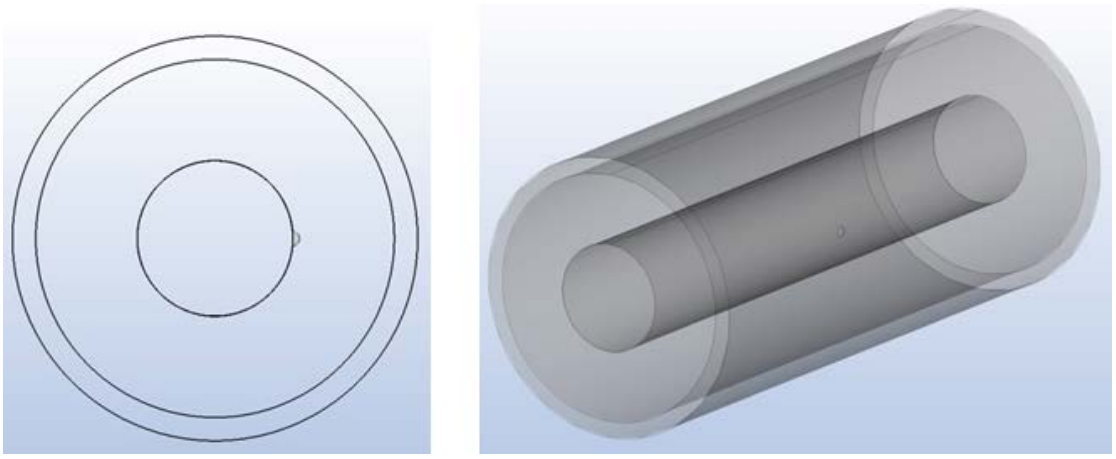

Figure 72 Defective Cable Model

The simulation result for the electric field is shown below.

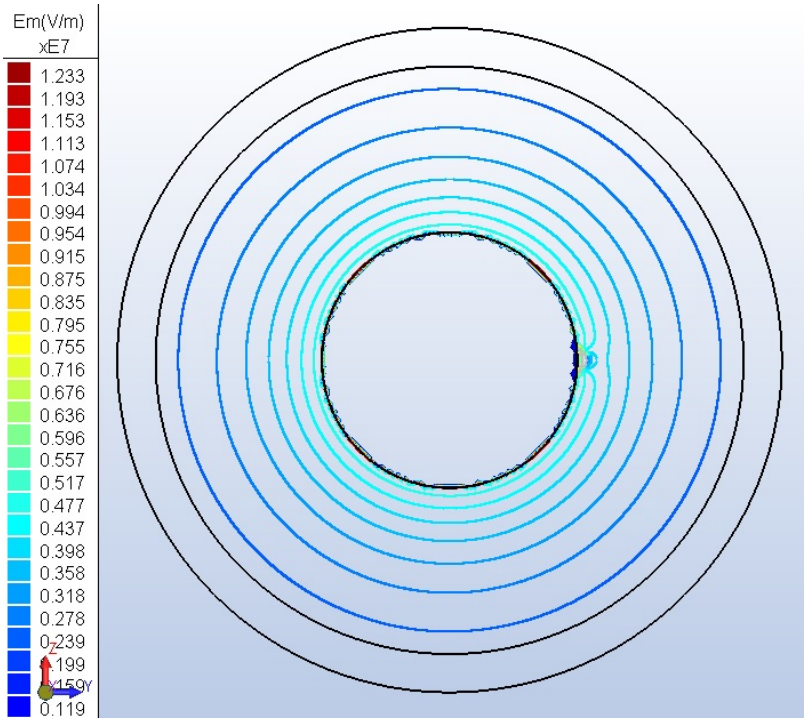

Figure 73 Electric Field of Defective Cable

The detail around the gap is shown in Figure 74. The electric field is higher around the defect, compared with intact situation. As a result, PD will be generated as long as the electric field around the defect is high enough.

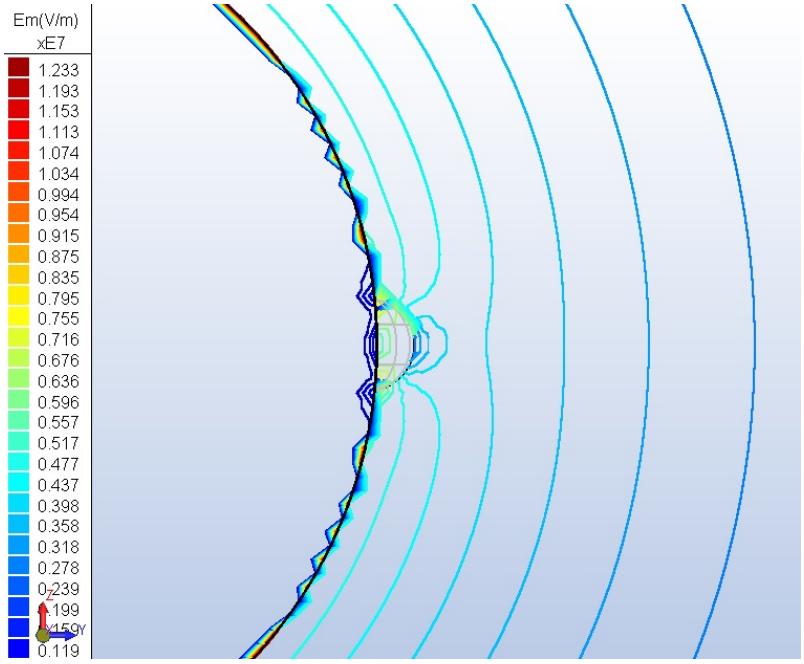

Figure 74 Detail Distribution

When the size of the gap is changed, this will contribute to the change in the electric field's intensity. There are four gap sizes (0.27 mm, 0.47 mm, 0.72 mm and 0.85 mm) and a no gap situation simulated. The electric fields from the center of the cable to the outside boundary of the cable are shown below.

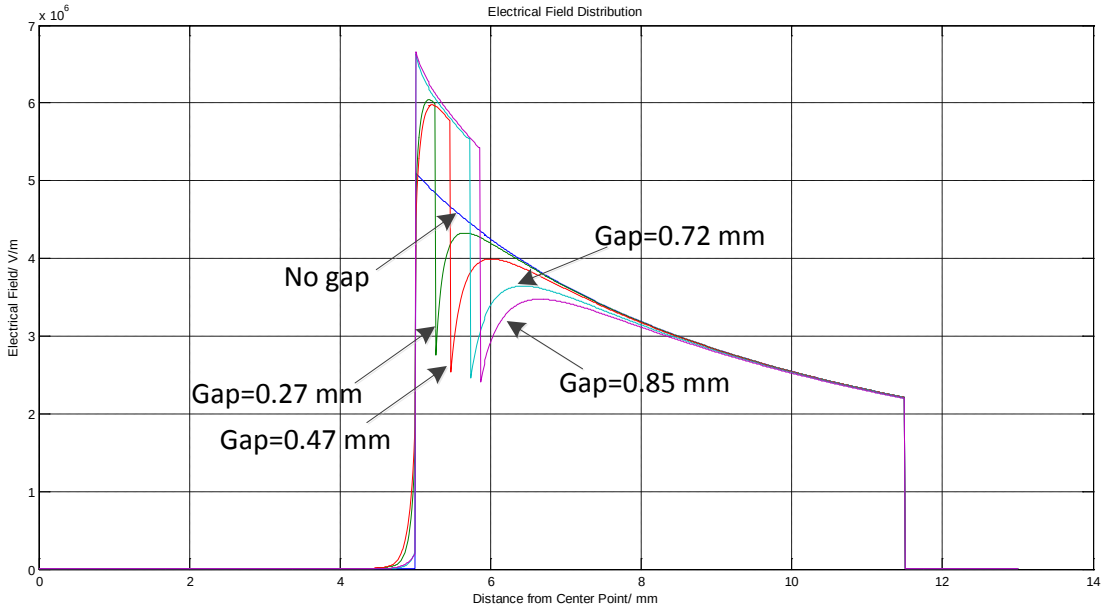

Figure 75 Electric Field Distribution of Different Gaps

5.3 Experiment System

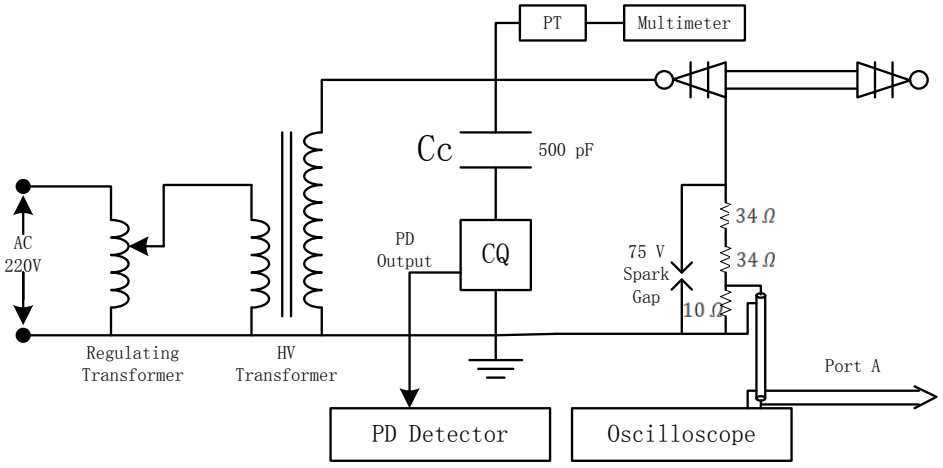

Figure 76 System Diagram for FBG-Based PD Sensor

The system diagram is shown in Figure 76. The conventional detection system is also combined in the circuit for comparison. Port A is connected with FBG-based PD sensor and supporting detection system. Its block diagram is shown in Figure 77.

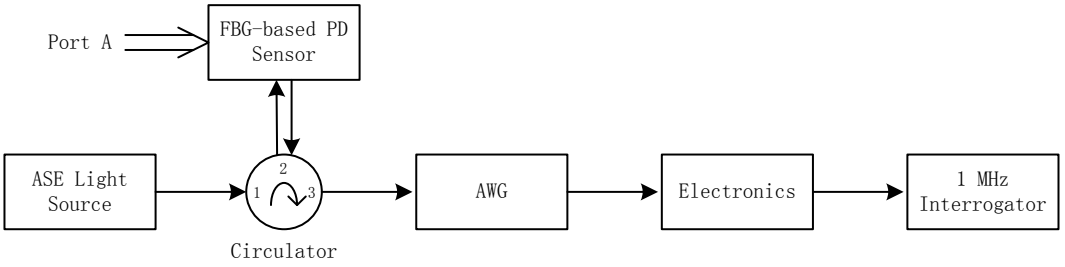

Figure 77 Block Diagram for Detection System with FBG-based PD Sensor

The piezoelectric ceramic transducer in the sensor can convert the small PD signal coming from Port A to pressure signal. The FBG is very sensitive to pressure signal, and the wavelength of light transporting inside its optical fiber has a relationship with intensity of pressure. The light coming from the amplified spontaneous emission (ASE) light source is modulated by the FBG-based PD sensor and then transferred to the arrayed waveguide gratings (AWG) by a circulator. Finally, the signals import 1 MHz interrogator through the electronics. The wavelength can be observed and recorded by SBench5. Two piezoelectric ceramic transducers are used in this experiment, one with a resonant frequency of 42.7 kHz and the other 300 kHz, products of EBL Products.

5.4 Pre-Test of Cable

To make sure there are PDs inside the cable, a pre-test was administered by utilizing a conventional detection system. The high voltage applied to the cable was varied gradually, and the PD magnitude was noted. The results are shown in Table 6.

Table 6 Test Results

Voltage/kV	PD/pC
3	2.3
4	2.3
5	2.3
6	2.3
7	2.4
8	2.6
9	3.0
10	3.3
11	4.1
12	6.3
13	10.2
14	19.3
15	24.3

The background noise is about 2.3 pC during the test. From Table 3.1, it is clear that PD can be seen above 7 kV (2.4 pC) and the PD is about 24.3 pC at 15 kV.

To make sure the PD is not generated from the connection to the cable, a corona camera, CoroCAM_III, was used. No external corona was observed, confirming that the PD was generated in the cable assembly, probably primarily in the splice, which is known to contain some defects.

5.5 Tests and Results

5.5.1 Test with 42.7 kHz PD Sensor

1. Direct Test with PD sensor

Since PDs can be observed above 7 kV with the conventional detection system, supplied voltage should be larger than 7 kV to make sure there are PDs in the cable. In addition to that, a control group is necessary for the comparing situations with PDs. This means that control group represents a situation without PDs (0 kV). Finally, tests under three voltage levels which represent control group (0 kV) and experiment groups (10 kV

and 13 kV) were conducted. Results are shown below. The recording time is 500 ms.

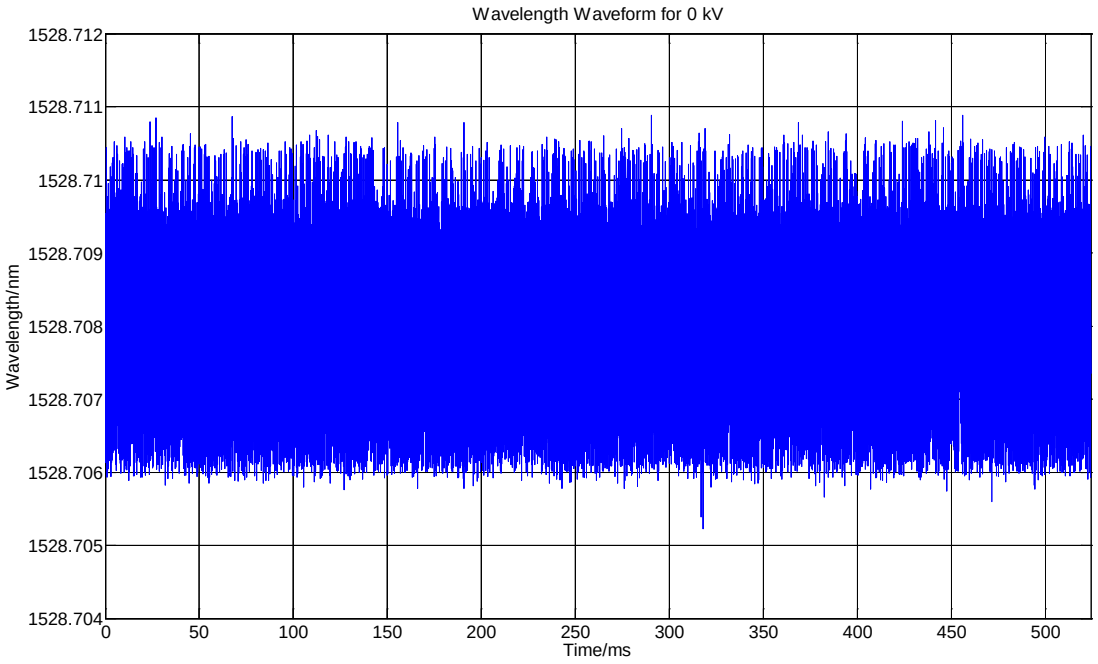

Figure 78 Wavelength Waveform for 0 kV

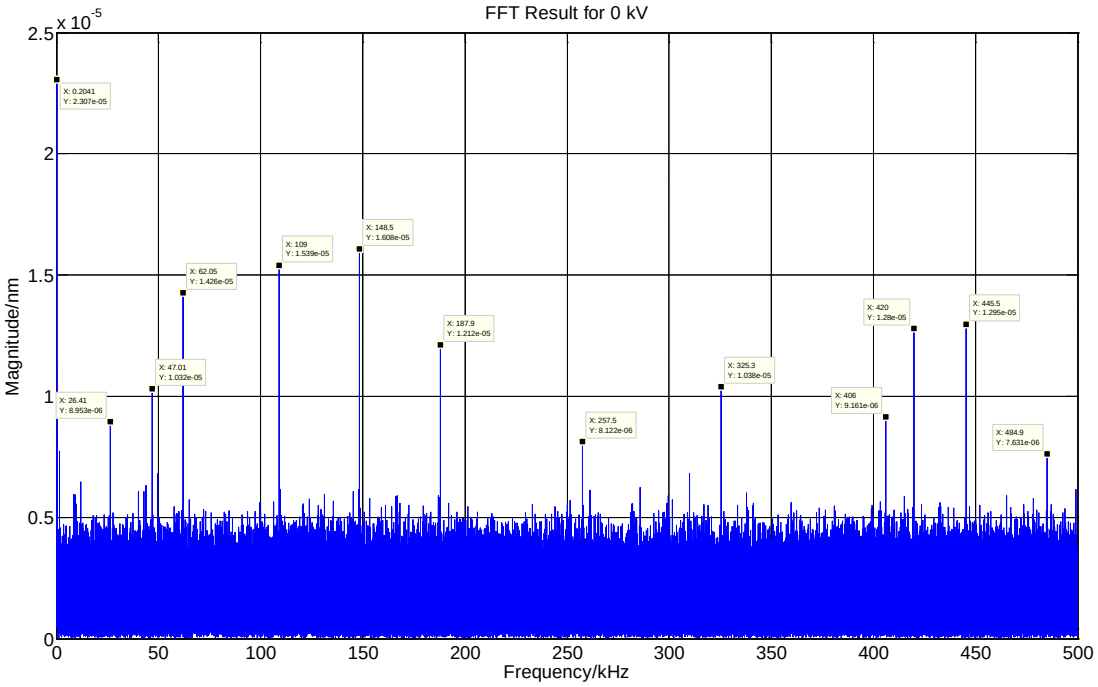

Figure 79 FFT Result for 0 kV

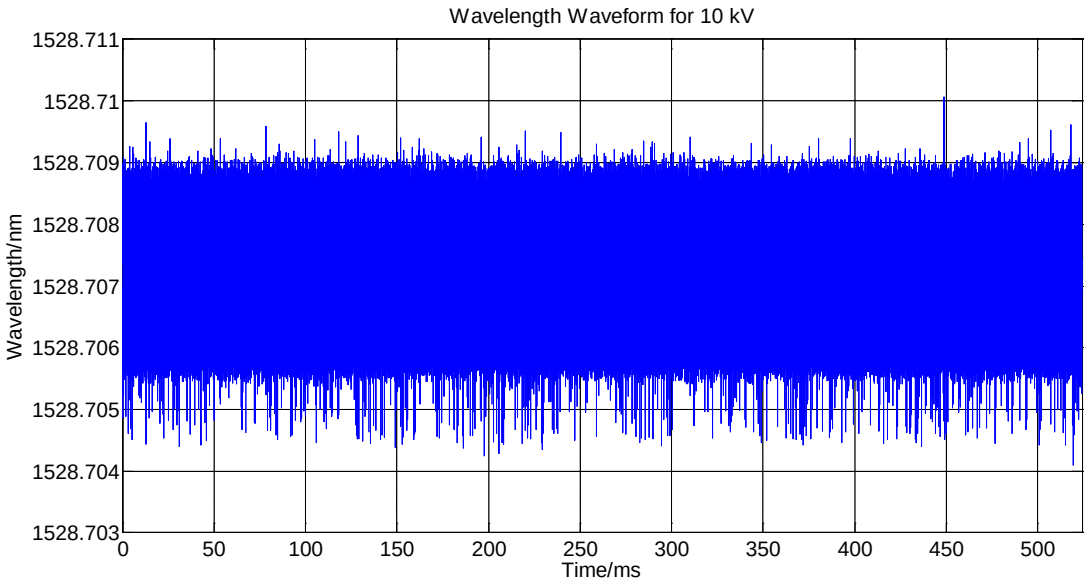

Figure 80 Wavelength Waveform for 10 kV

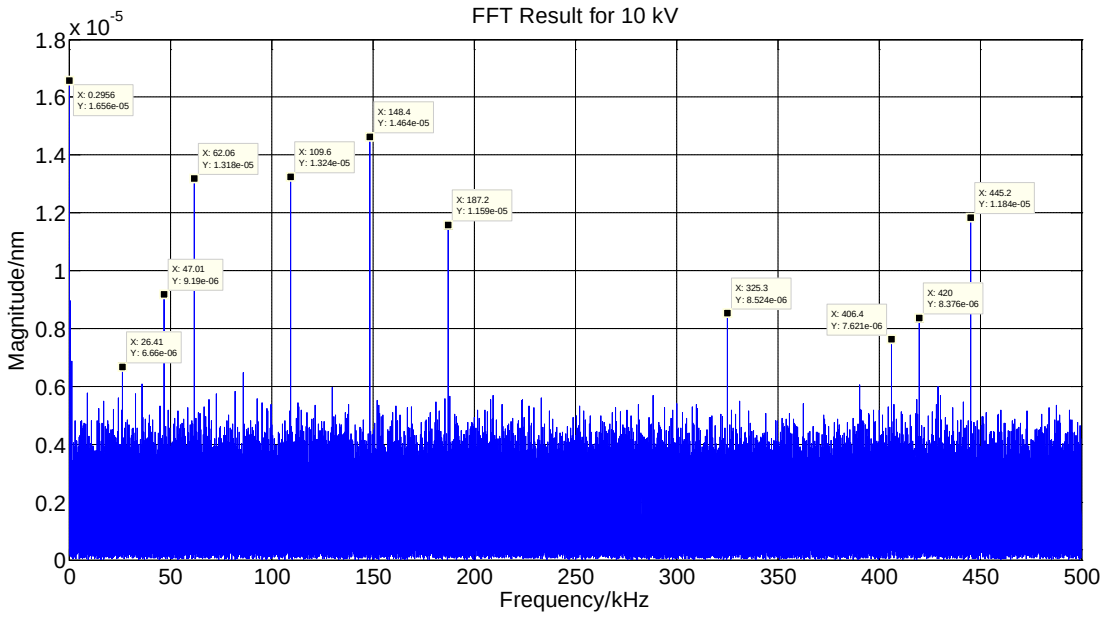

Figure 81 FFT Result for 10 kV

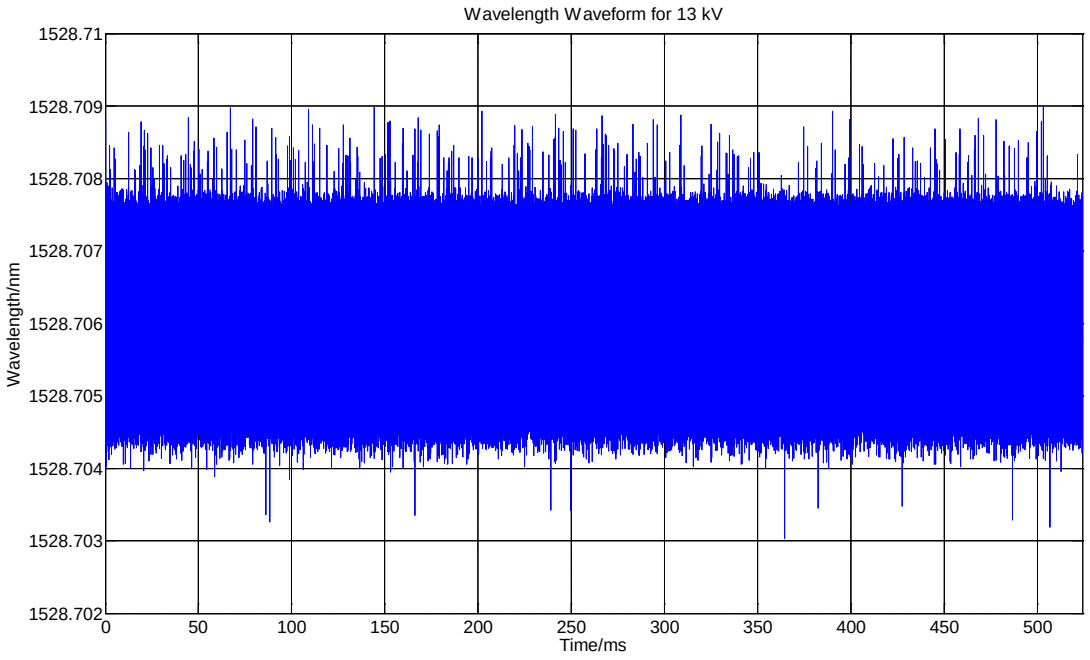

Figure 82 Wavelength Waveform for 13 kV

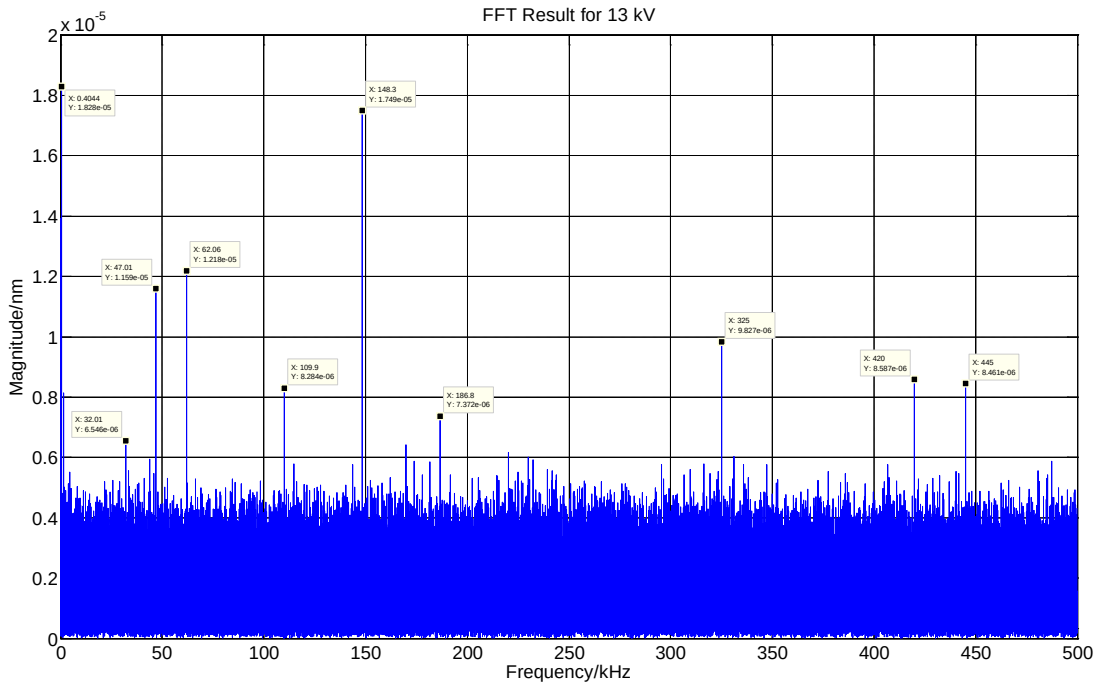

Figure 83 FFT Result for 13 kV

There are some apparent values in all three FFT plots, all of which occur at certain frequencies without tendency for the magnitudes. There is a high probability that these

noticeable values are noises, because their frequencies do not change and no value is recorded around 42.7 kHz.

2. Test with High-Pass Filter

Since no result is observed before, C_k, PD Detector and oscilloscope have been removed to reduce possible interferences in this test. Meanwhile, to remove low frequency components, a high-pass filter was added to the circuit, which has a cutoff frequency of 8 kHz.

The magnitude response of the high pass filter is shown in Figure 84.

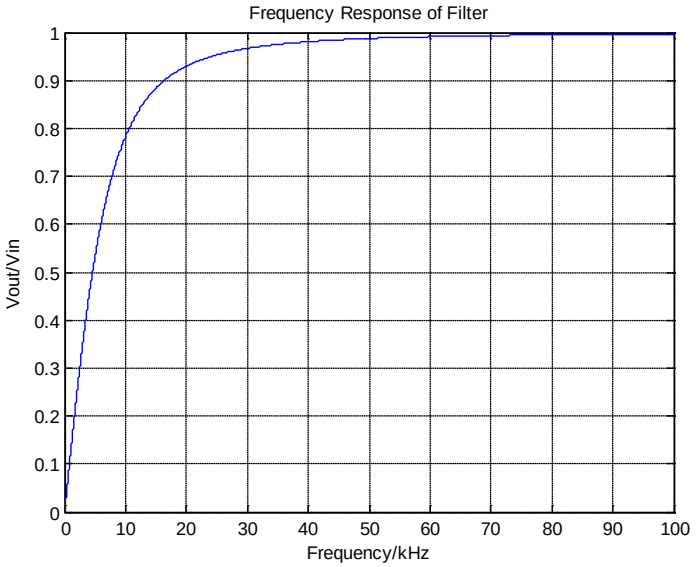

Figure 84 Frequency Response of High Pass Filter

Three voltage levels (0 kV, 5 kV and 13 kV) have been applied to the cable. The results are shown below.

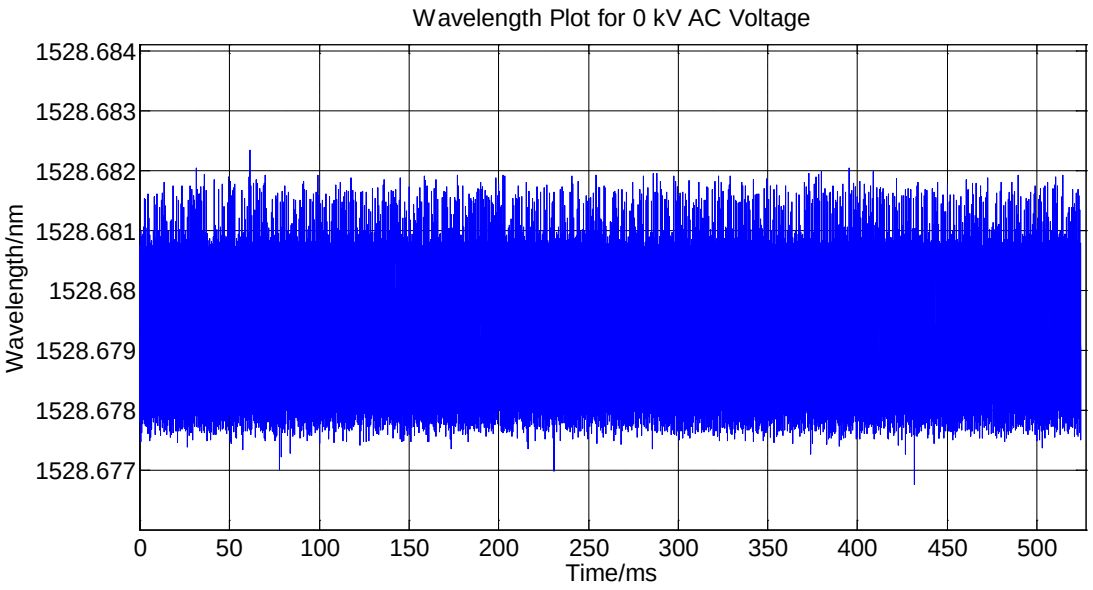

Figure 85 Wavelength Waveform for 0 kV

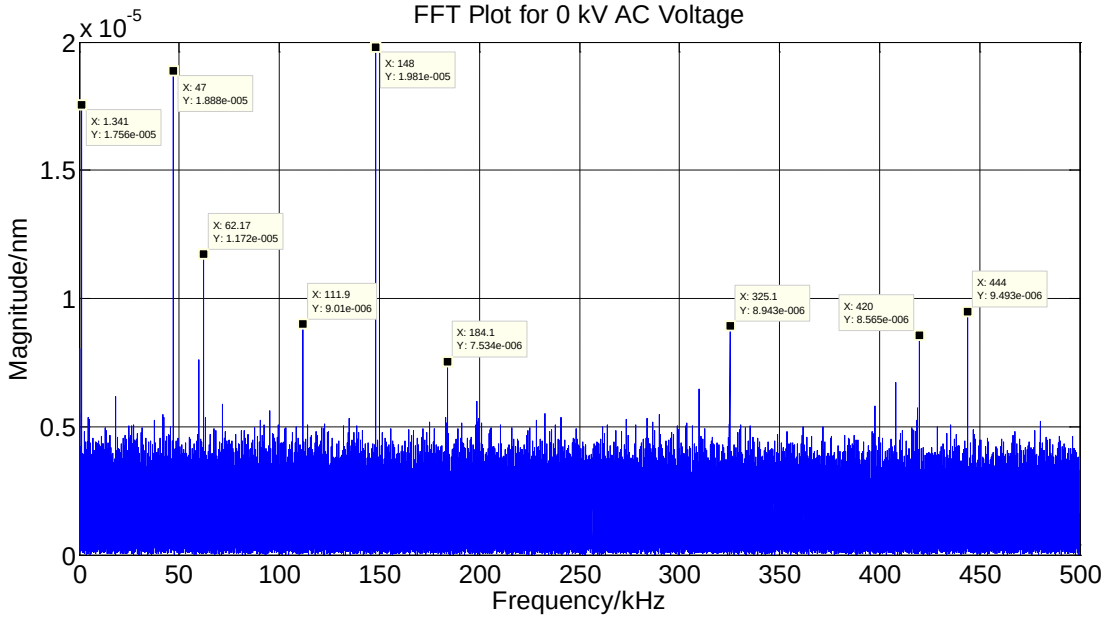

Figure 86 FFT Result for 0 kV

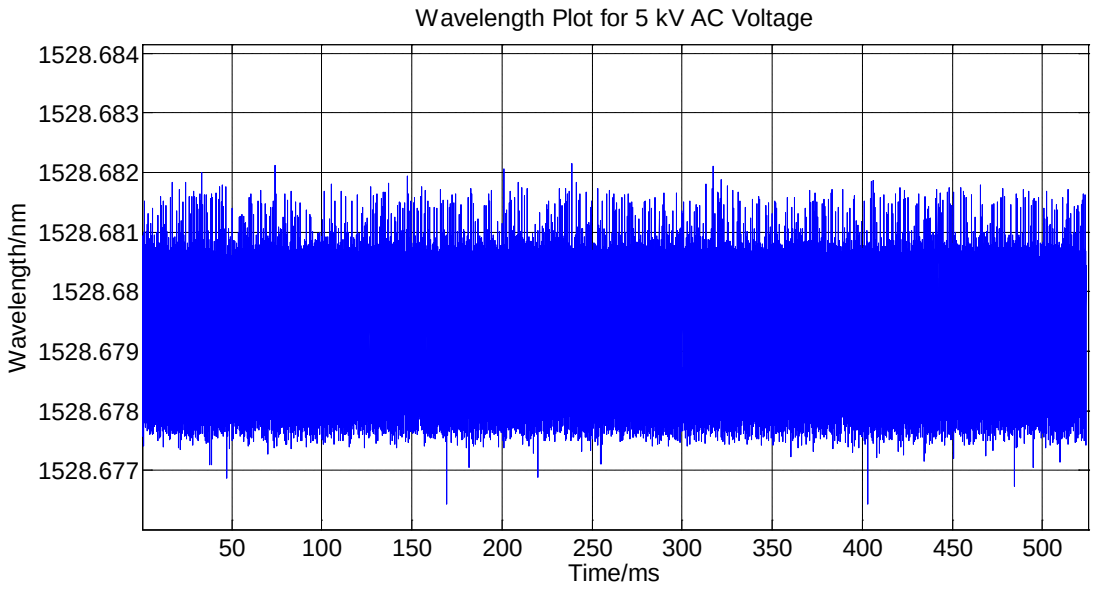

Figure 87 Wavelength Waveform for 5 kV

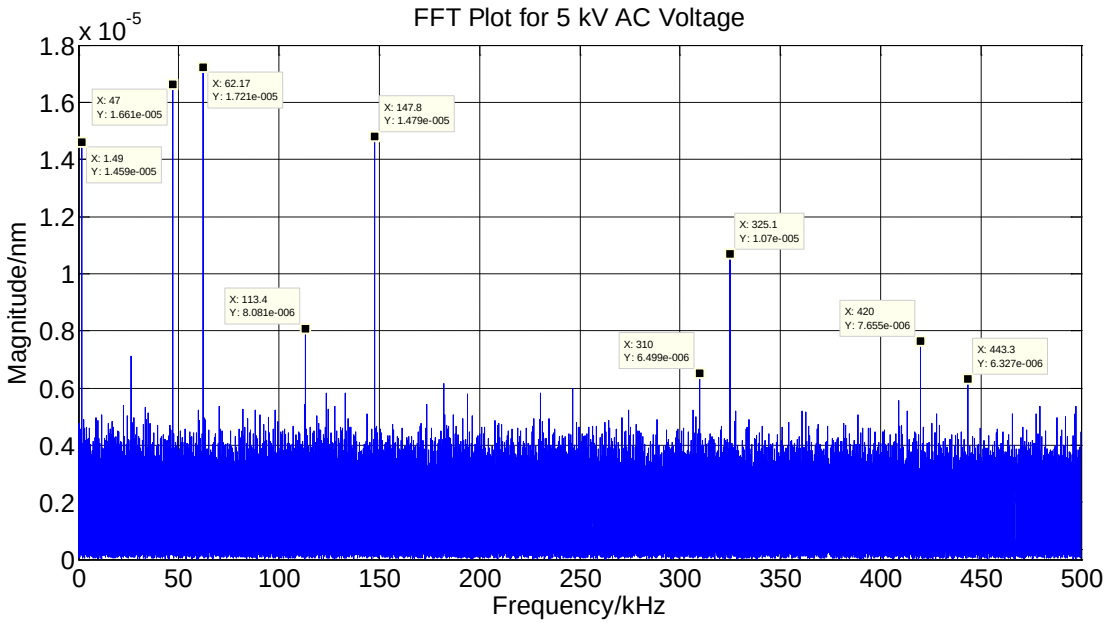

Figure 88 FFT Result for 5 kV

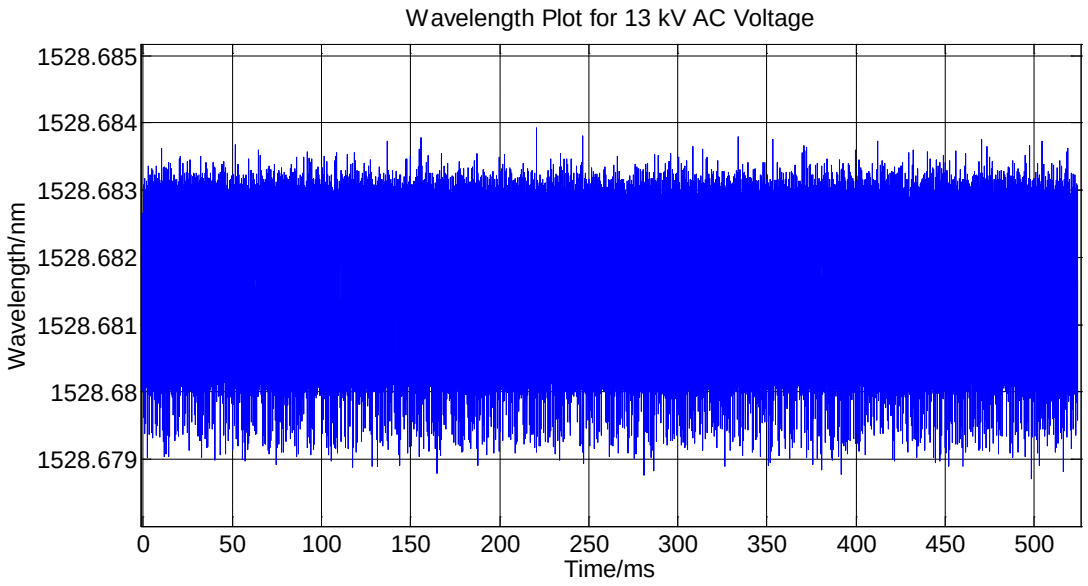

Figure 89 Wavelength Waveform for 13 kV

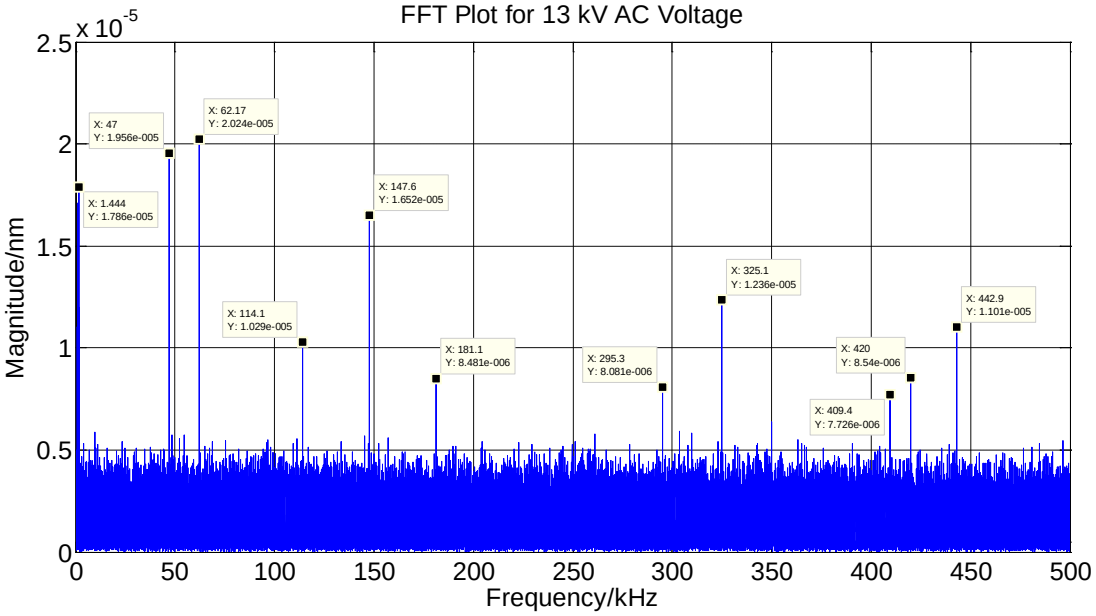

Figure 90 FFT Result for 13 kV

Compared with previous tests, some noticeable values in FFT results disappear. However, for the rest of the parts, the values stay the same and there is no increase or decrease trend.

3. Test with Band-Pass Filter

Since the resonant frequency is 42.7 kHz, a band-pass filter was utilized to study the details around this frequency. The system diagram is the same with that in Figure 76 but it replaced the high pass filter with the band-pass filter. The magnitude response of the band-pass filter is shown in Figure 91.

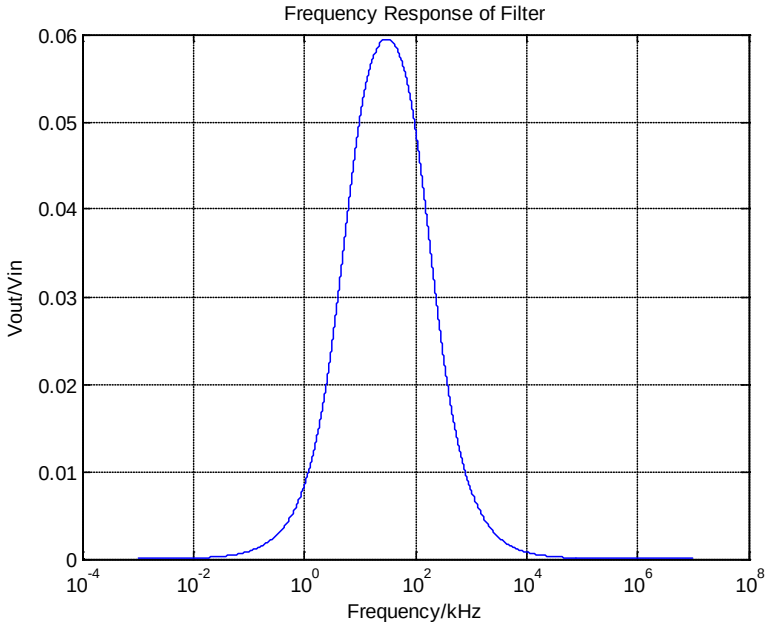

Figure 91 Frequency Rresponse of Band-Pass Filter

Three voltage levels (0 kV, 5 kV and 13 kV) were applied to the cable. The results are shown below.

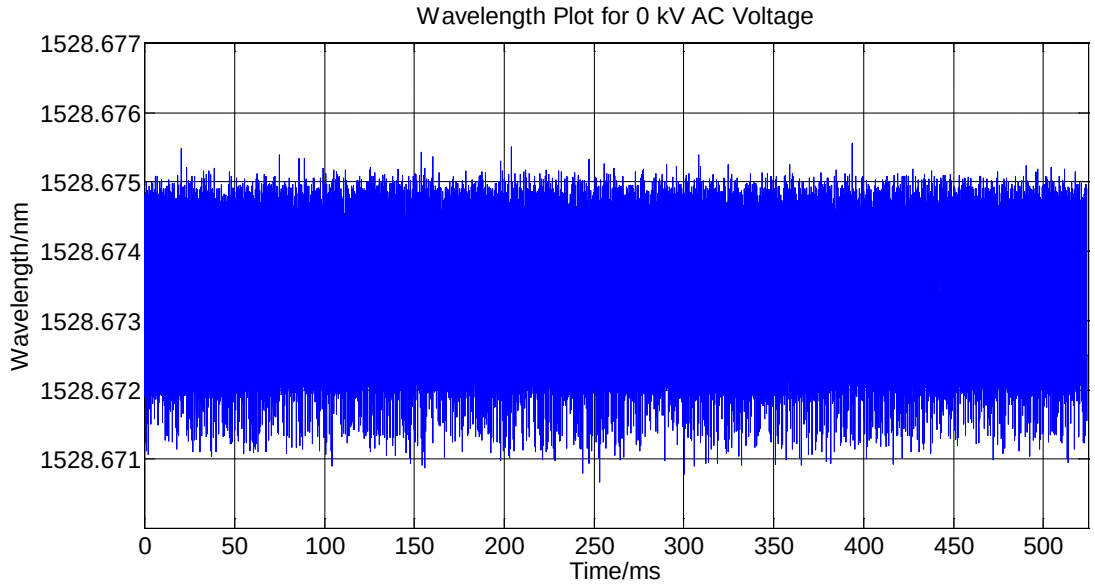

Figure 92 Wavelength Waveform for 0 kV

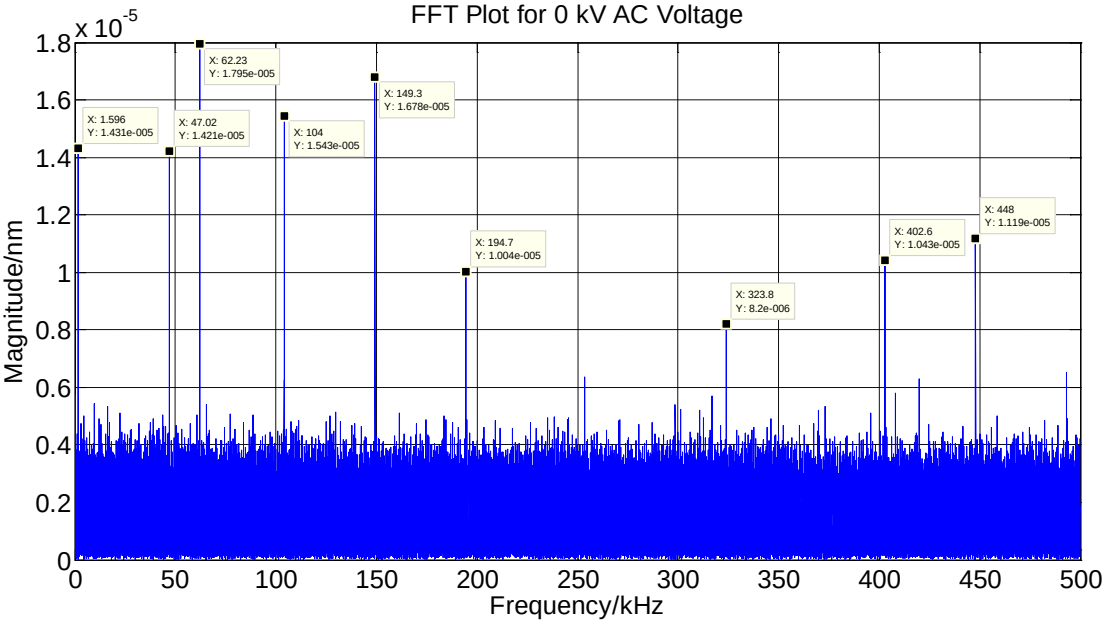

Figure 93 FFT Results for 0 kV

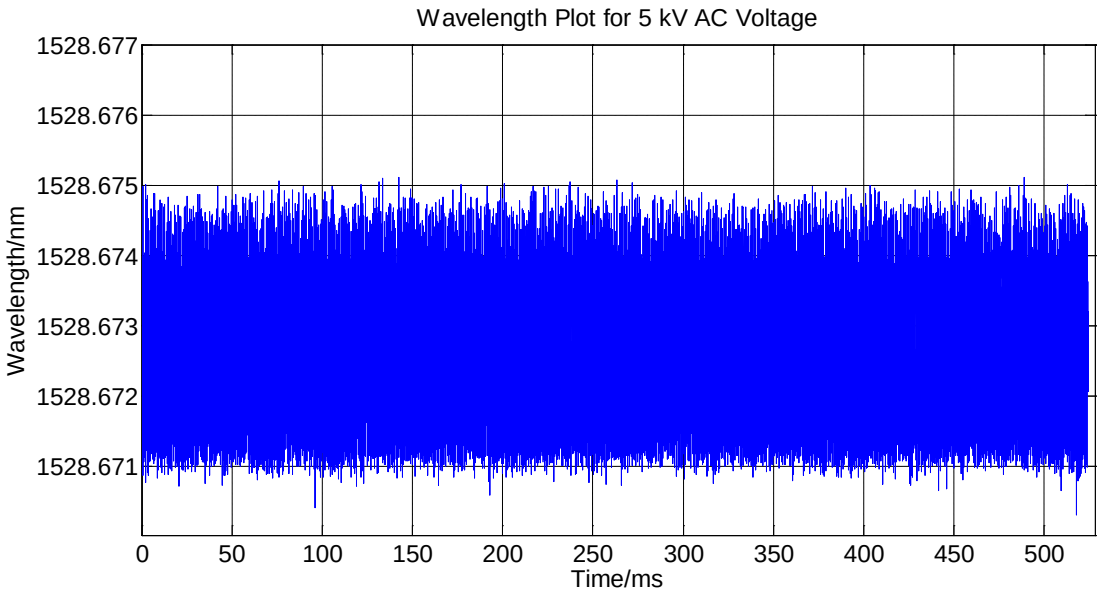

Figure 94 Wavelength Waveform for 5 kV

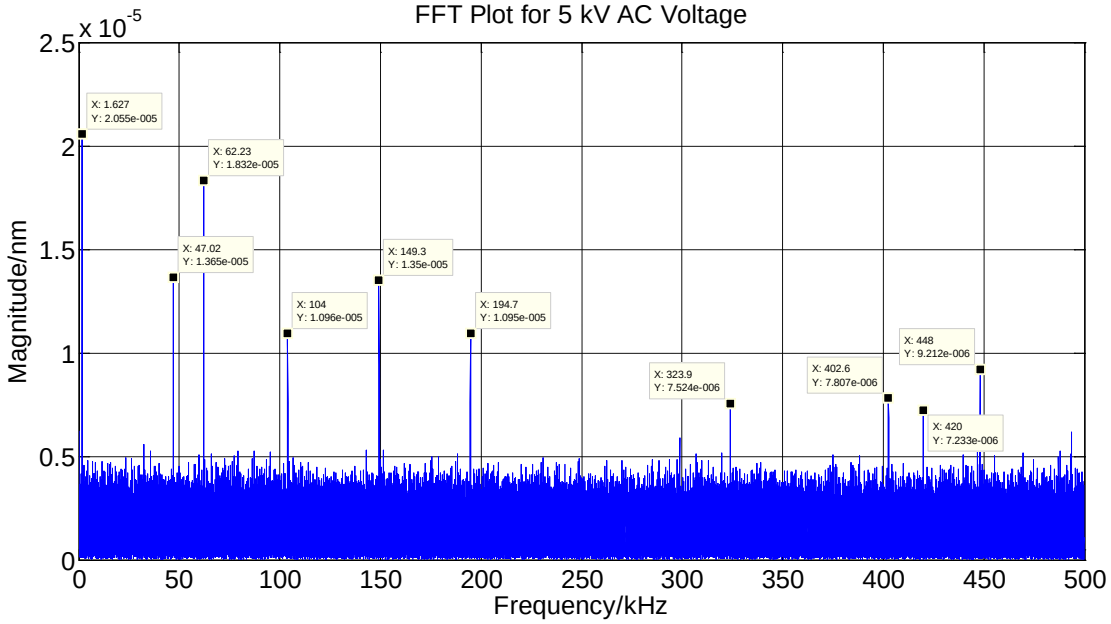

Figure 95 FFT Result for 5 kV

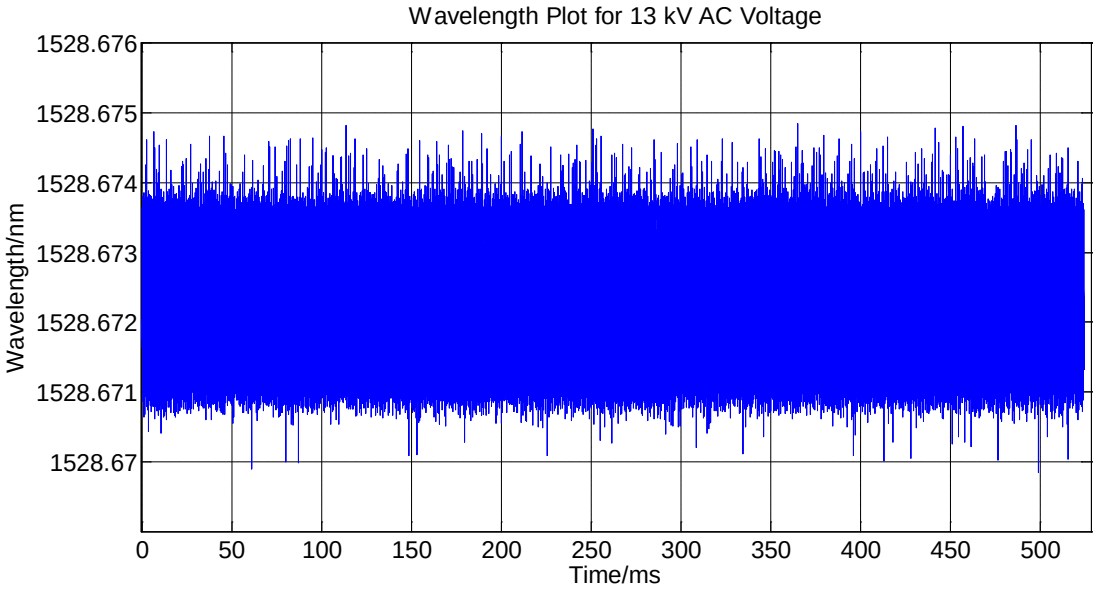

Figure 96 Wavelength Waveform for 13 kV

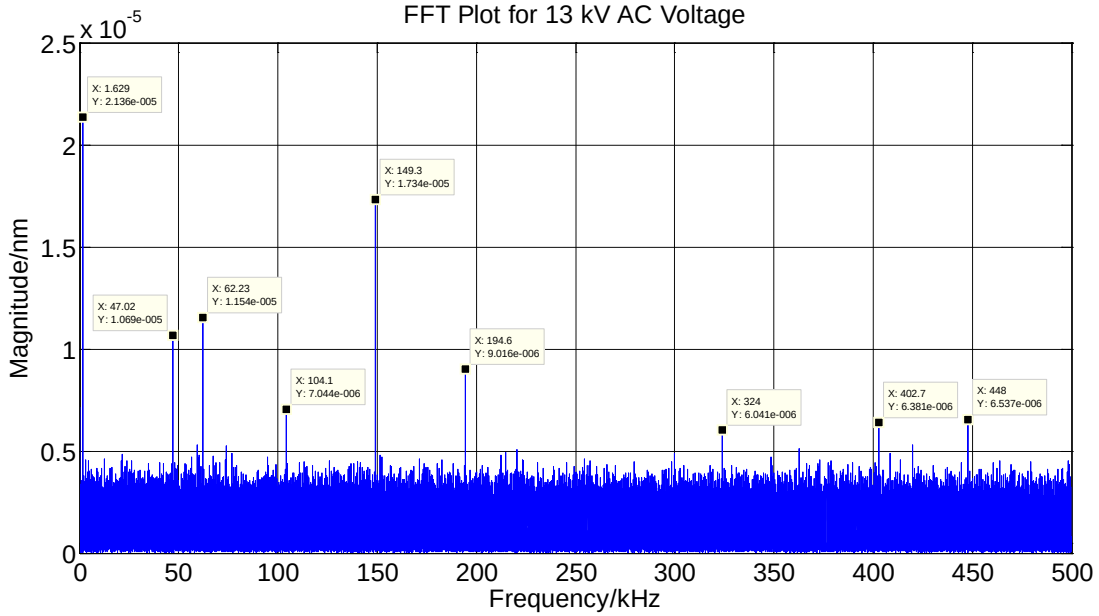

Figure 97 FFT Result for 13 kV

There is still no tendency can be found in all FFT result plots, even when a band-pass filter is utilized.

4. Test with Digital Filter

It is hard to build a band-pass filter with a very narrow bandwidth. Therefore a

digital filter was used to get a narrower bandwidth around 42.7 kHz which is beneficial to study the details. The data processing was done in Simulink with an infinite impulse response (IIR) band-pass filter. The magnitude response is shown in Figure 98.

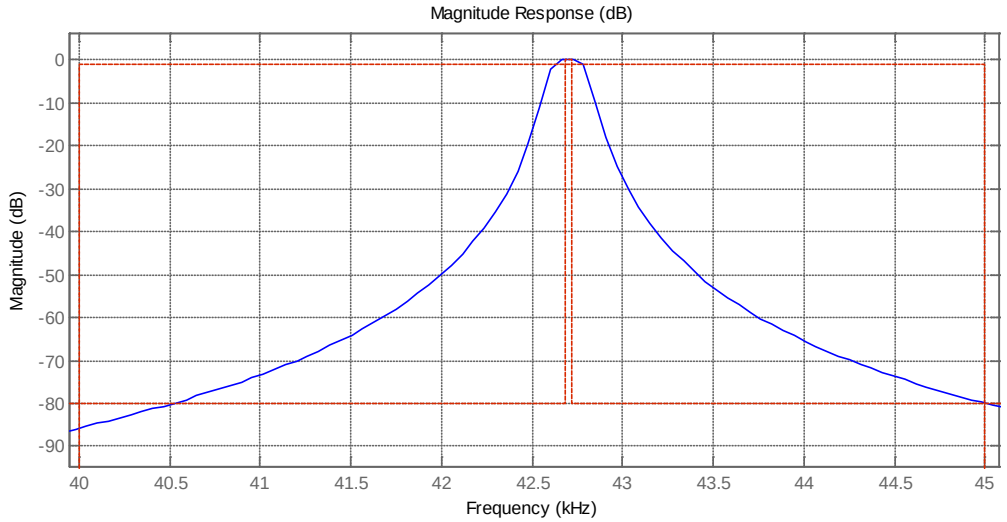

Figure 98 Frequency Response of IIR Filter

Three voltage levels (0 kV, 5 kV and 13 kV) were applied to the cable and wavelength waveforms after IIR filter are shown below.

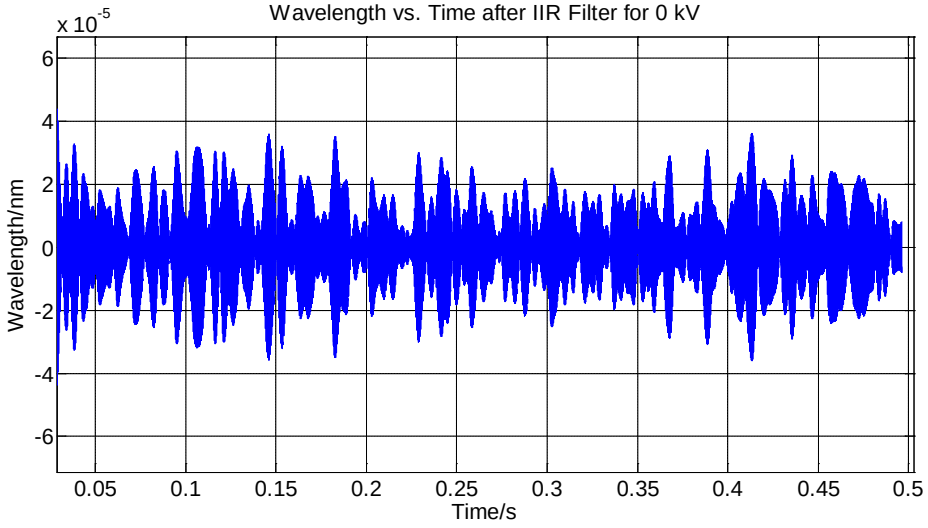

Figure 99 Wavelength Waveform for 0 kV

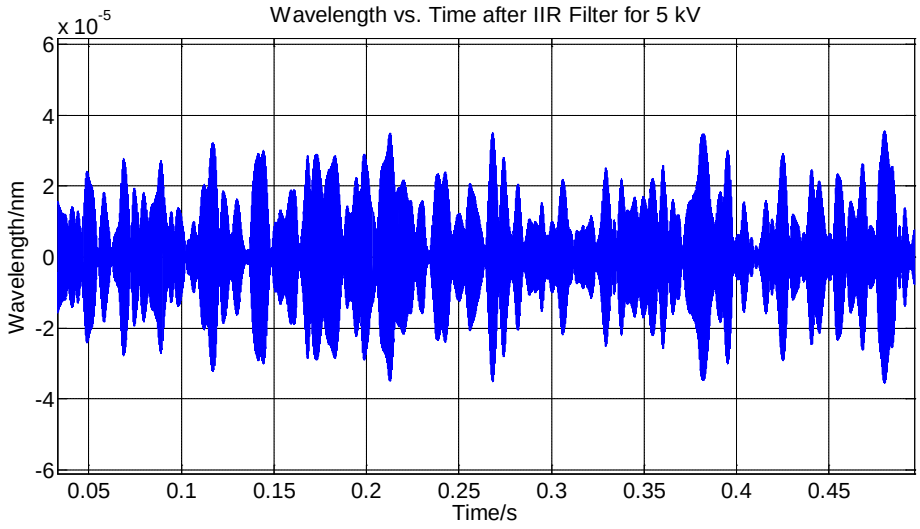

Figure 100 Wavelength Waveform for 5 kV

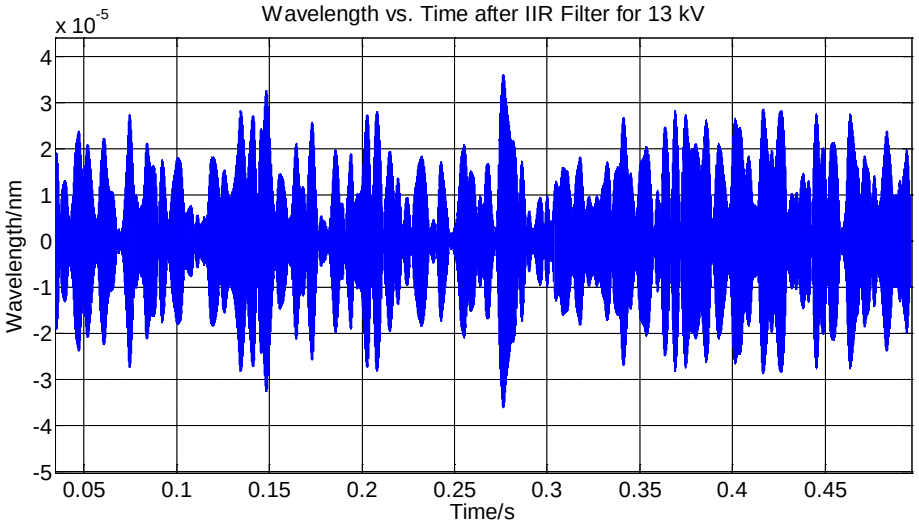

Figure 101 Wavelength Waveform for 13 kV

The bandwidth is so narrow that it is unnecessary to do FFT analysis. RMS and Peak-Peak (P-P) values of the output waveform are shown in Table 7.

Table 7 RMS and P-P Values with IIR Filter

Voltage Level/kV	RMS Value/nm	P-P Value/nm
0	1.14×10^{-5}	7.20×10^{-5}
5	1.08×10^{-5}	7.22×10^{-5}
13	1.16×10^{-5}	7.11×10^{-5}

It is obvious that no trend appears for both RMS and P-P values for the output waveforms, even with a much narrower band-pass filter.

5. Test without Electronics

The more complex the system is, the more noise sources there are. The electronics was removed from the test system to reduce the potential noise.

RMS and P-P values are shown in Table 8. However, no tendency is observed.

Table 8 RMS and P-P Values without Electronics

Voltage Level/kV	RMS Value/nm	P-P Value/nm
0	5.67×10^{-6}	3.80×10^{-5}
5	5.37×10^{-6}	3.72×10^{-5}
13	6.31×10^{-6}	3.99×10^{-5}

6. Test without 1MHz Interrogator

The 1 MHz interrogator was also removed to reduce noise. A DC component was found when the experiments were conducted without an interrogator. For the data in Table 9, the DC component is removed since what being concerned are the AC components. This DC component is the output of the average light wavelength which is not interested and discharge signals are reflected by the change in wavelength which is the AC components. By analyzing signals both before and after the filter, there is no trend at all.

Table 9 RMS and P-P Values without 1MHz Interrogator

Voltage	Before Filter		After Filter	
Level / kV	P-P Value / V	RMS Value / V	P-P Value / V	RMS Value / V
0	0.0017	2.91×10^{-4}	3.70×10^{-5}	5.01×10^{-6}
5	0.0013	2.01×10^{-4}	4.00×10^{-5}	4.76×10^{-6}
13	0.0012	1.09×10^{-4}	1.48×10^{-5}	2.60×10^{-6}

5.5.2 Sensor's Response to Impulse

To show the response of FBG-based sensor to impulse, there were five signals to be tested, one of which is a no impulse situation and the others with impulse magnitudes of 0.11626 V, 0.28503 V, 0.57305 V and 1.1595 V. All these impulse signals come from the calibration part inside the PD detector and are connected directly with the sensor. The

waveform of 1.1595 V impulse is shown in Figure 102. The rest of these impulses have the same wave shape with magnitude as the only difference. Figure 103 below is a real PD signal in Cable.

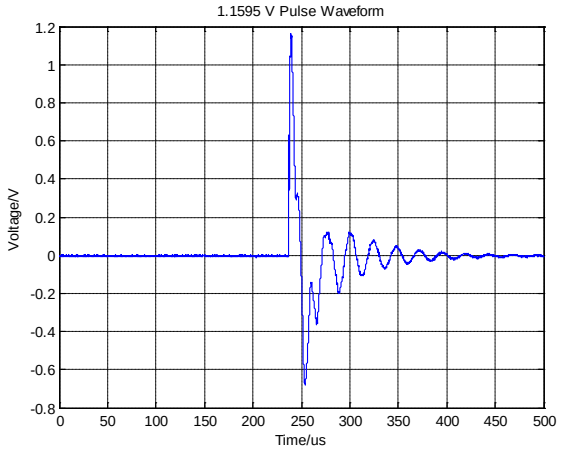

Figure 102 1.1595 V Pulse Waveform

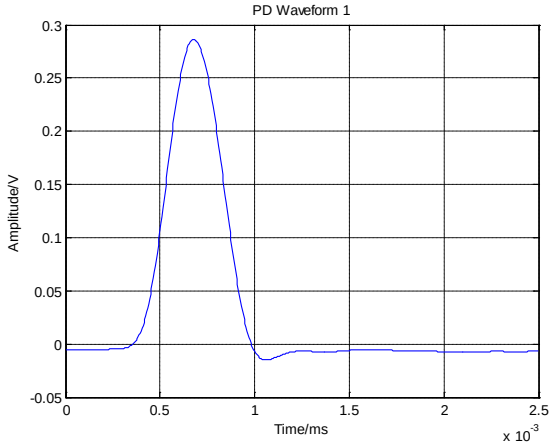

Figure 103 Real PD Signal in Cable

The test results are shown in the following figures. The length of the recording time is 16.384 ms.

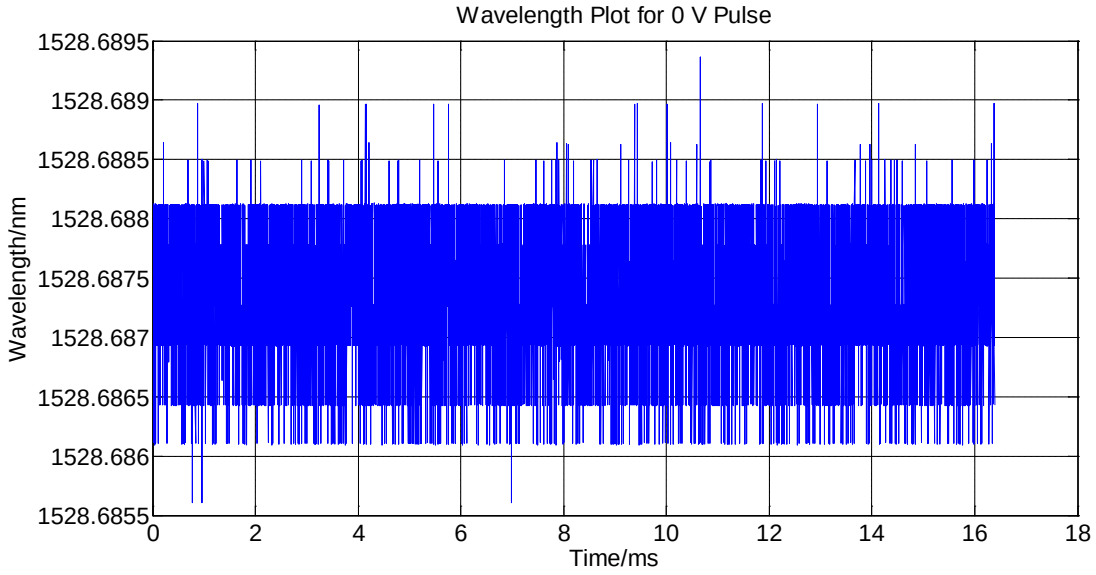

Figure 104 Wavelength Waveform for No Signal

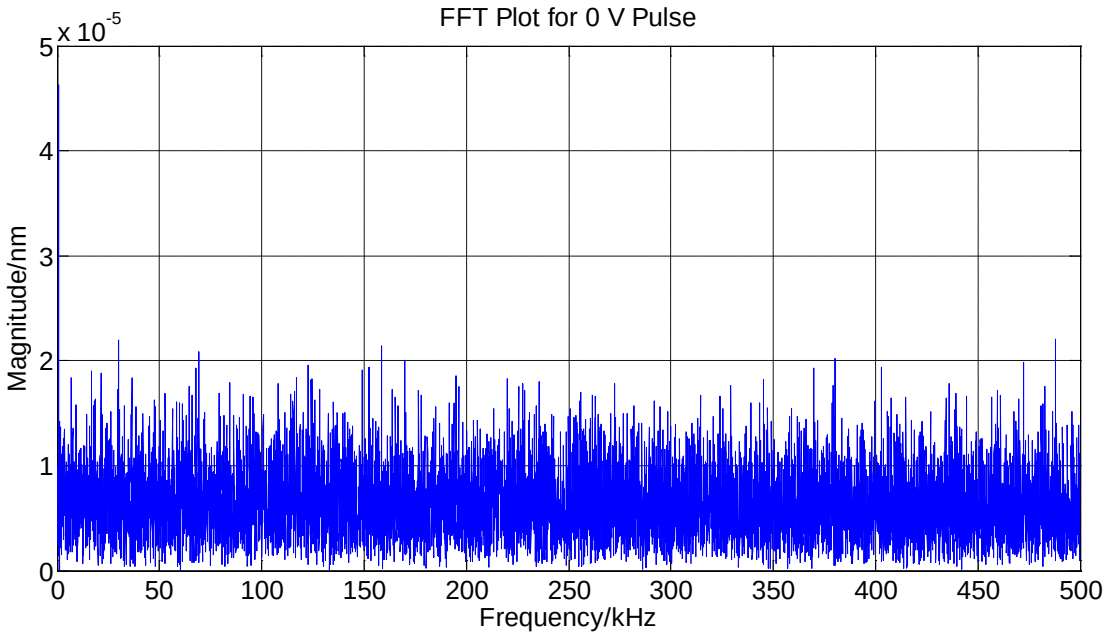

Figure 105 FFT Result for No Signal

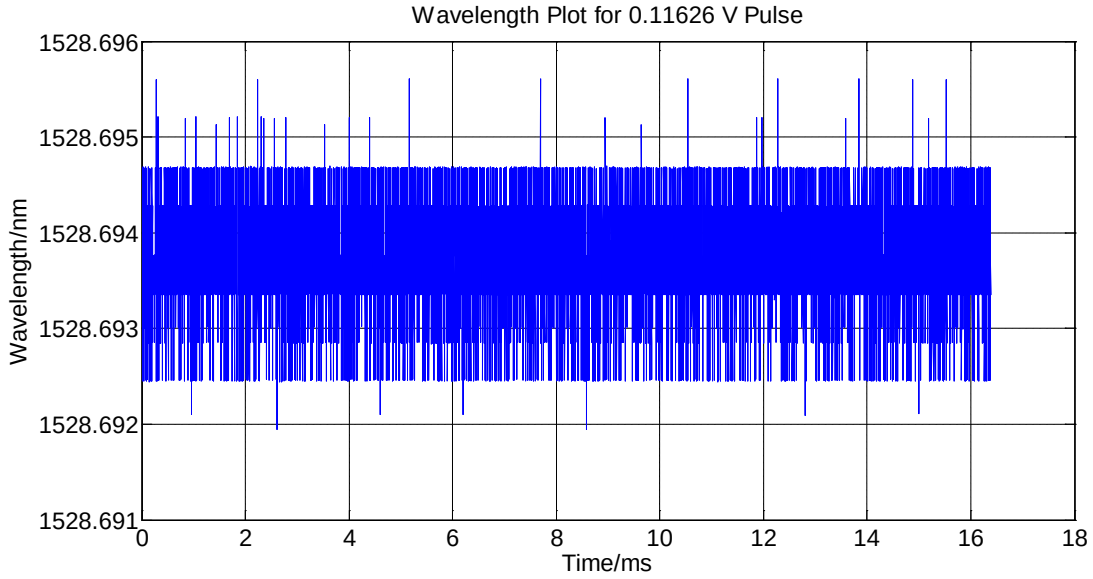

Figure 106 Wavelength Waveform for 0.11626 V Pulse

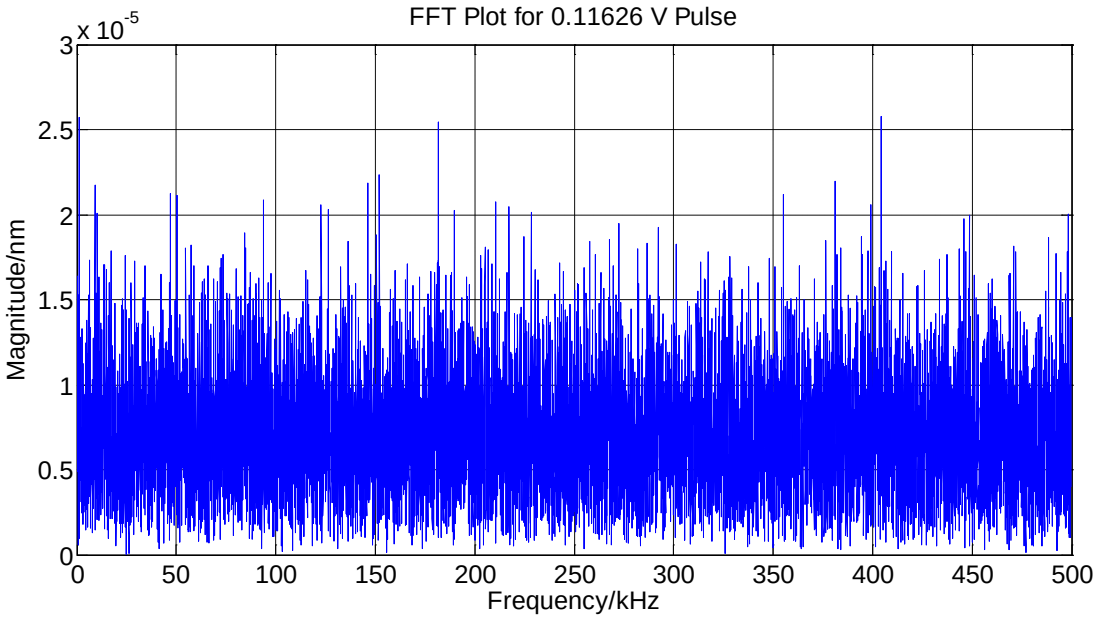

Figure 107 FFT Result for 0.11626 V Pulse

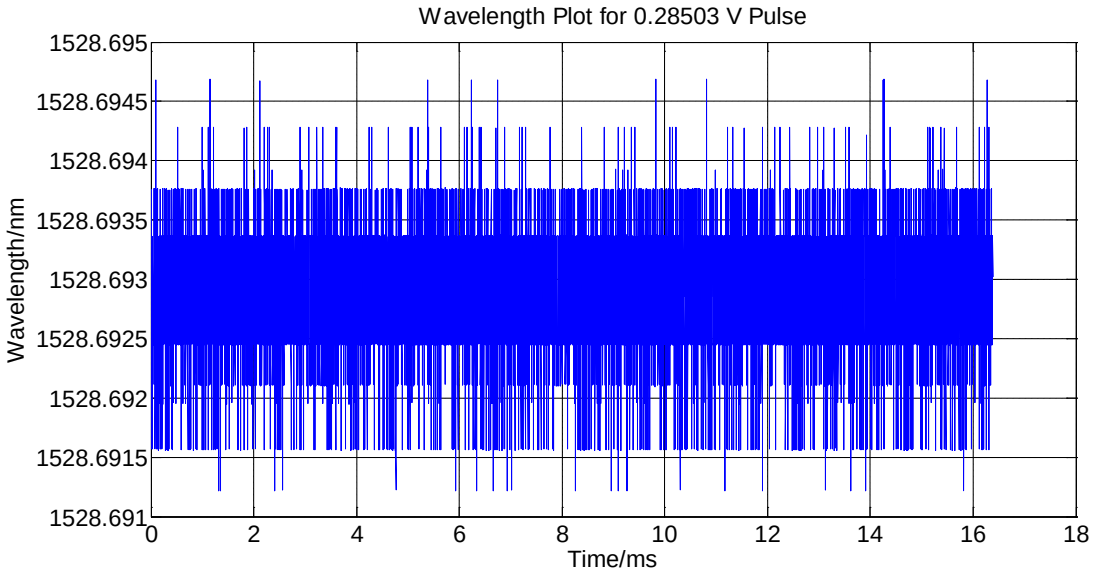

Figure 108 Wavelength Waveform for 0.28503 V Pulse

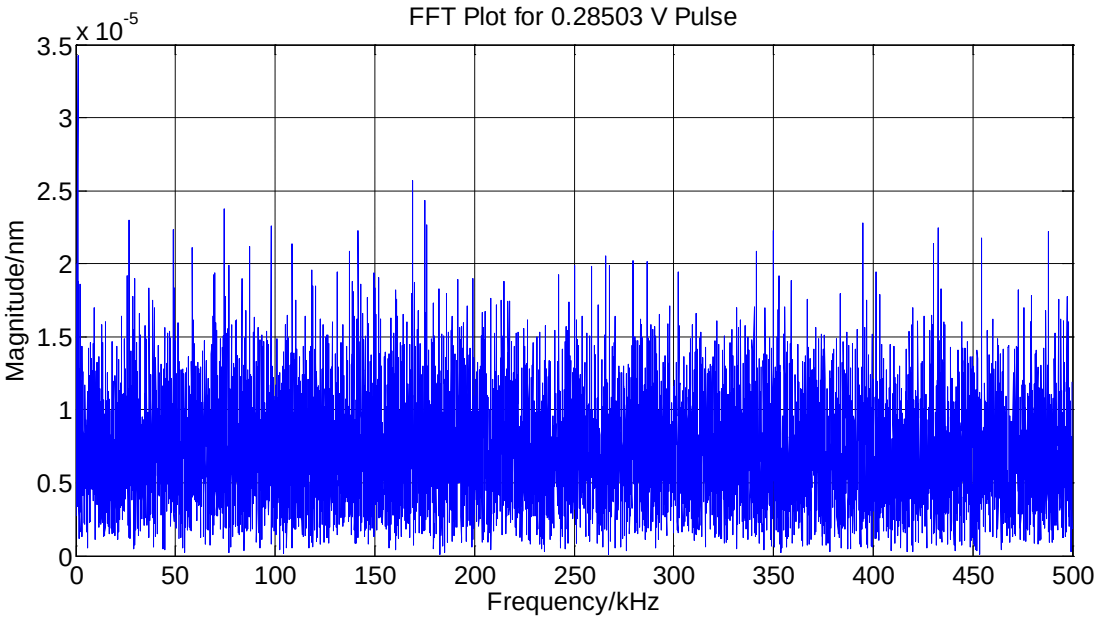

Figure 109 FFT Result for 0.28503 V Pulse

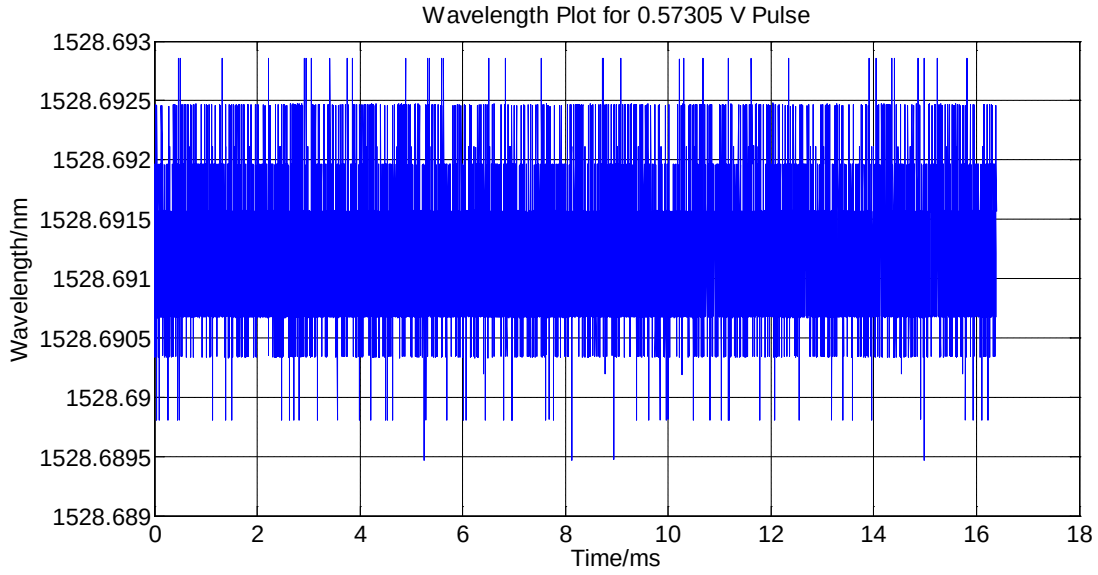

Figure 110 Wavelength Waveform for 0.57305 V Pulse

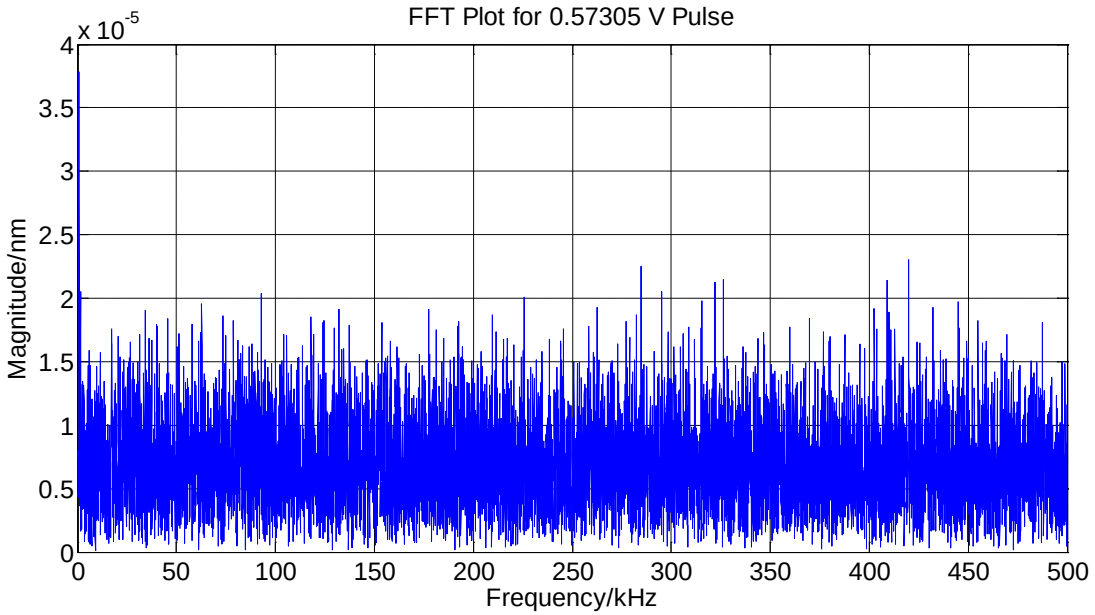

Figure 111 FFT Result for 0.57305 V Pulse

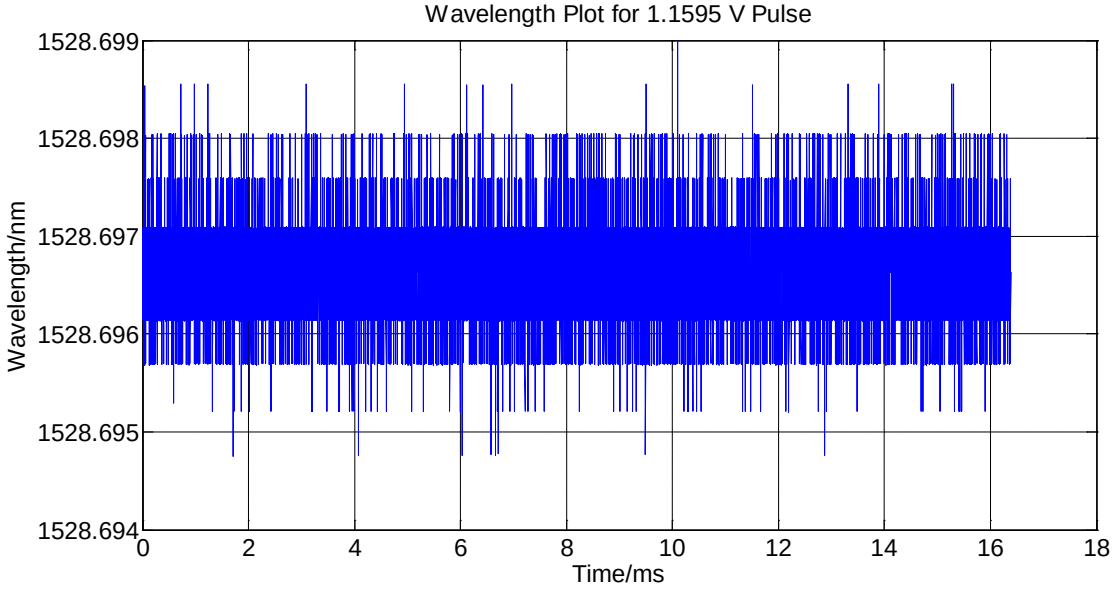

Figure 112 Wavelength Waveform for 1.1595 V Pulse

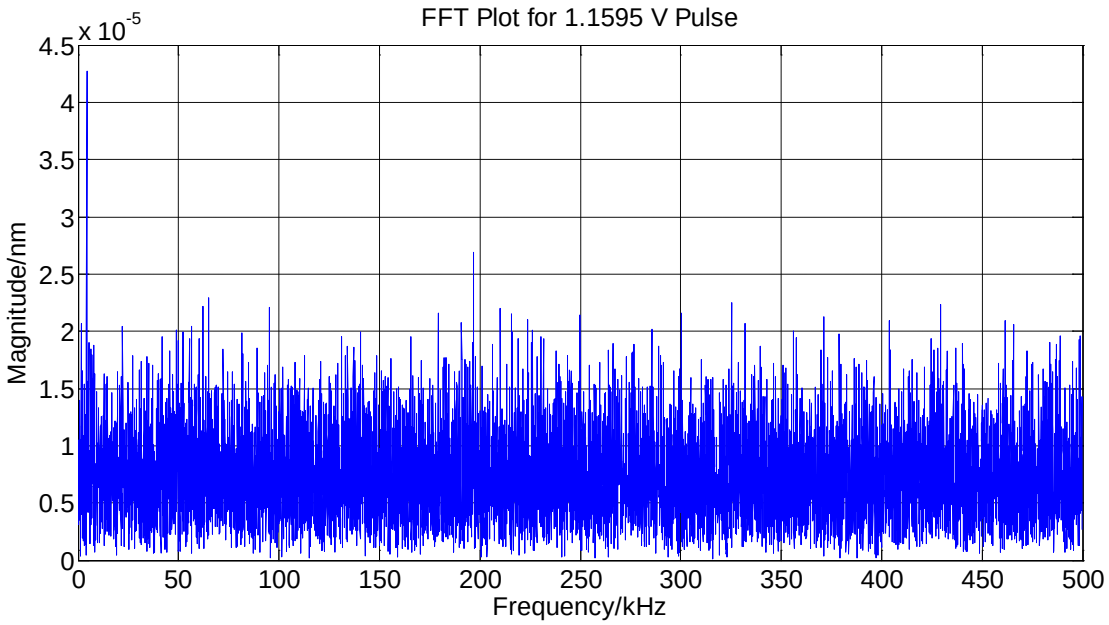

Figure 113 FFT Result for 1.1595 V Pulse

It can be seen that no matter how large the magnitude is, the FBG-based PD sensor do not have the ability to detect the impulse signal.

5.5.3 Test with 300 kHz PD Sensor

1. Analysis of Data before Filter

Larger supplied voltages were used this time. The RMS and P-P values are shown in Table 10.

Table 10 RMS and P-P Values before IIR Filter

Voltage Level/V	0	5	15	20
P-P Value/nm	5.98×10^{-4}	5.43×10^{-4}	5.56×10^{-4}	5.04×10^{-4}
RMS Value/nm	1542.55	1542.55	1542.55	1542.55

2. Analysis of Data after IIR Filter

IIR filter, whose -3dB frequencies are 299.05 kHz and 300.05 kHz, was utilized to extract information at around 300 kHz. The magnitude response of IIR filter is shown in Figure 114.

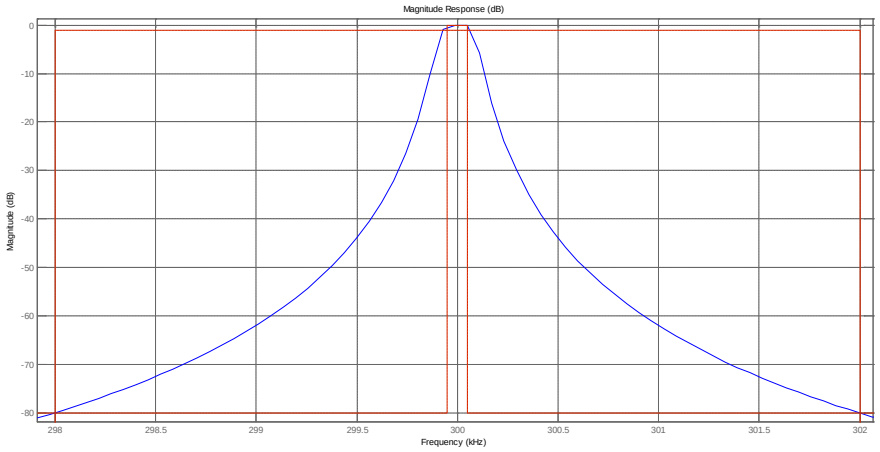

Figure 114 Magnitude Response for 300 kHz IIR Filter

The RMS and P-P values are shown in Table 11.

Table 11 RMS and P-P Values after IIR Filter

Voltage Level/V	0	5	15	20
P-P Value/nm	4.28×10^{-6}	3.67×10^{-6}	3.76×10^{-6}	4.11×10^{-6}
RMS Value/nm	5.97×10^{-7}	6.03×10^{-7}	5.86×10^{-7}	6.09×10^{-7}

3. Analysis of Data from Oscilloscope without IIR Filter

Since oscilloscope's analog bandwidth is up to 1 GHz, which is much higher than the resonant frequency of Piezoelectric Ceramic Transducer used in the sensor; details that cannot be captured by FBG-based PD sensor can be recorded by oscilloscope. This happens because the lower sampling rate can lose high frequency components. The sample rate is set to be 250 Mpts/s while the recording time is 100 ms.

The RMS and P-P values are shown in Table 12.

Table 12 RMS and P-P Values from Oscilloscope without IIR Filter

Voltage Level/V	0	5	15	20
P-P Value/nm	0.67×10^{-3}	0.67×10^{-3}	0.67×10^{-3}	0.67×10^{-3}
RMS Value/nm	0.0018	0.0018	0.0018	0.0018

4. Analysis of Data from Oscilloscope with IIR Filter

The RMS and P-P values are shown in Table 13.

Table 13 RMS and P-P Values from Oscilloscope with IIR Filter

Voltage Level/V	0	5	15	20
P-P Value/nm	1.67×10^{-8}	1.55×10^{-8}	2.06×10^{-8}	1.97×10^{-8}
RMS Value/nm	1.36×10^{-9}	1.34×10^{-9}	1.35×10^{-9}	1.36×10^{-9}

5. Analysis of Oscillation Gotten by Oscilloscope

When recording data directly with oscilloscope, high magnitude oscillations were occasionally observed. One is recorded and shown in Figure 115. This oscillation is recorded at 15 kV.

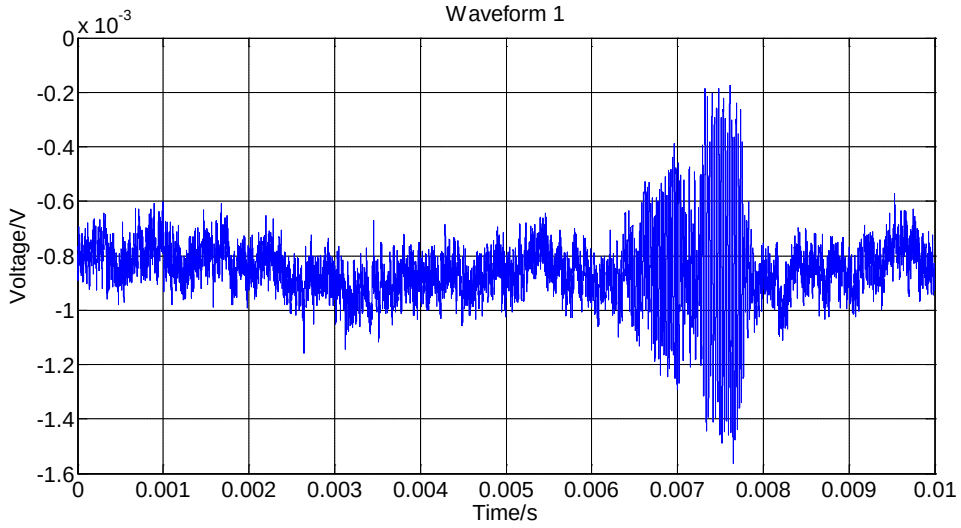

Figure 115 High Magnitude Oscillation obtained by Oscilloscope

This oscillation did not appear every cycle but happened at intervals between a few cycles. There is a high probability that this oscillation is caused by certain kind of partial discharges. One assumption is that this kind of PD is coupling with the PD sensor and causes a significant oscillation. The FFT result is shown in Figure 116.

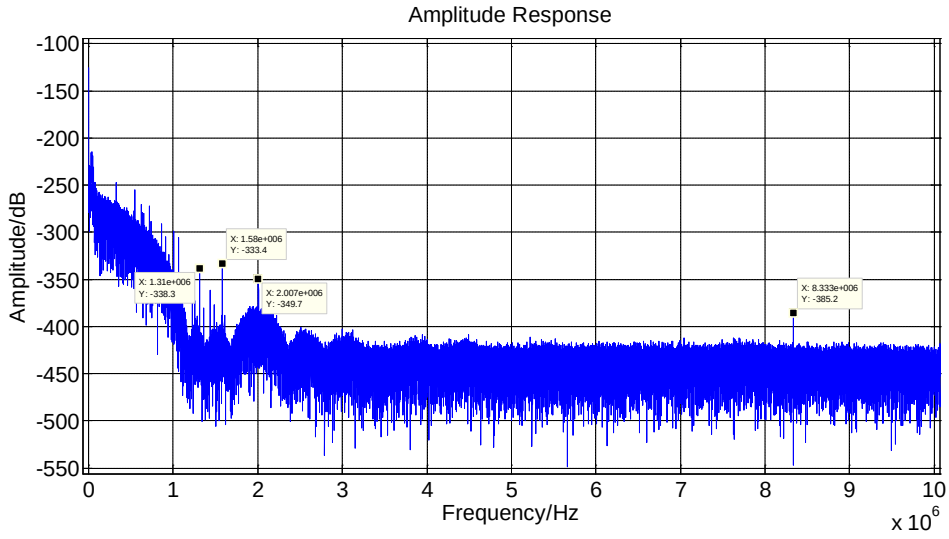

Figure 116 FFT Result for Oscillation under 15 kV

5.5.4 Discussion

Even testing the detection system by utilizing many methods, for 42.7 kHz FBG-based PD sensors, there is no evidence to show that the detection system picks up any PD signal. However, with 300 kHz sensor, oscillations are observed. These oscillations may be caused by PDs with certain frequency that can resonate with the sensor. But no further information to verify whether they are PD signals. In this situation, sweep-frequency measuring setup can be a good choice to verify whether this oscillation is caused by PDs.

Chapter 6

CONCLUSIONS AND FUTURE WORK

6.1 Conclusions

The main objective of the research is to utilize pulse sequence analysis method classify different types of discharges and explore the behavior of a new detection system with FBG-based PD sensor.

Conventional PD detection method is used to find out factors that can affect PD values in Rod-Plane Model. ANOVA and time-frequency map are employed to analyze the PD values at different rod diameters, gap distances and voltage levels. ANOVA analysis reveals that rod diameter and gap distance have influence on PD value but voltage level do not. Time-frequency map cannot reveal any trend when rod diameters or gap distances are modified. However, it shows differences among types of discharges. Therefore, for the same type of discharge, there is almost no difference in PDs. However, the characteristics of different types of discharges are significant enough to make classification.

A series of Rod-Plane Models are built in Coulomb to understand the electric field distribution. The electric field will increase with the increasing of gap distances and decrease with the increasing of rod diameters. Furthermore, high electric field is mainly concentrated near the tip of the rod. The electric field strength will decrease rapidly when going far away from the tip of rod.

In pulse sequence analysis, two distribution graphs, $\Delta u/\Delta\varphi$ and $\Delta u(i+1)/\Delta u(i)$, have been used to classify different types of discharges. The results show that these two graphs have a high degree of consistency for the same type of discharge. There

is almost no difference when changing rod diameters or gap distances. On the other hand, the differences between two types of discharges are significant. Therefore, both two graphs can be used to categorize discharges.

For the new detection system with FBG-based PD sensor, two piezoelectric ceramic transducers are used, one with resonant frequency of 42.7 kHz and the other 300 kHz. The output of two FBG-based PD sensors could not be correlated with conventional method. However, there are some oscillations when observing with oscilloscope for 300 kHz sensor. The reason may be that these PDs have a certain frequency and can resonate with the 300 kHz FBG-based PD sensor. Unfortunately, due to the limitation of the detection system and cable sample, it could not be verified whether they are caused by a certain kind of PDs since the recording of PD signal with FBG-based PD sensor is not synchronous with the recording of conventional method.

6.2 Future Work

There are some topics that can be further pursued for future researches regarding Pulse Sequence Analysis method and FBG-based PD sensor. The followings are the suggestions for future works:

- Utilizing pulse sequence analysis method with other discharge sources to verify its ability to classify different types of discharges.
- Utilizing pulse sequence analysis method with different detection systems for the same kind of partial discharges to verify its consistency in distribution patterns.
- Utilizing 300 kHz FBG-based PD sensor to other types of PDs to verify whether those oscillations are caused by PD signals.

- Searching for an appropriate piezoelectric ceramic transducer with wider bandwidth so that the FBG-based PD sensor has the ability to cover all PD frequency range.

REFERENCES

[1] Ir F.H. Kreuger, Partial Discharge Detection in High-Voltage Equipment, butterworth, 1989

[2] A. A. Al-Arainy, N. H. Malik and M. K. Al-Bahloul, “Statistical Variation of AC Corona Pulse Amplitudes in Point-to plane Air Gaps,” IEEE transactions on Electrical Insulation, August 1989, Vol. 24, No. 4, pp. 681-687.

[3] Steven A. Boggs, “Partial Discharge: Overview and Signal Generation,” IEEE Electrical Insulation Magazine, July/August 1990, Vol. 6, No. 4, pp. 33-39.

[4] Essay Wen Shu, Steven A. Boggs, “Effect of Dispersion on PD Pulse Propagation in Shielded Power Cable,” 2008 Annual Report Conference on Electrical Insulation Dielectric Phenomena, 26-29 Oct. 2008, pp. 427-430.

[5] S. A. Boggs, G. C. Stone, “Fundamental Limitations in the Measurement of Corona and Partial Discharge,” IEEE Transactions on Electrical Insulation, April 1982, Vol. EI-17, No. 2, pp. 143-150.

[6] A. M. Gaouda, Ayman EI-Hag, T. K. Abdel-Galil, M. M. A. Salama, R. Bartnikas, “On-line Detection and Measurement of Partial Discharge Signals in a Noisy Environment,” IEEE Transactions on Dielectrics and Electrical Insulation, Aug. 2008, Vol. 15, Issue. 4, pp. 1162-1173.

[7] A. Cavallini, G. C. Montanari, “A Fuzzy Logic Algorithm to Detect Electrical Trees in Polymeric Insulation Systems,” IEEE Transactions on Dielectrics and Electrical Insulation, December 2005, Vol. 12, No. 6.

[8] Steven Boggs, John Densley, “Fundamentals of Partial Discharge in the Context of Field Cable Testing”, IEEE Electrical Insulation Magazine, Sept.-Oct. 2000, Vol. 16, Issue. 5, pp. 13-18.

[9] M. T. G. Gillespie, G. B. Murchie, G. C. Stone, “Experience with AC Hipot and Partial Discharge Tests for Commissioning Generating Station Cables and Switchgear,” IEEE Transactions on Energy Conversion, September 1989, Vol. 4, No. 3.

[10] A. Cavallini, G. C. Montanari, F. Puletti, “A Novel Method to Locate PD in Polymeric Cable Systems Based on Amplitude-frequency (AF) Map,” IEEE Transactions on Dielectrics and Electrical Insulation, June 2007, Vol. 14, Issue. 3, pp. 726-734.

[11] S. A. Boggs, G. C. Stone, “Fundamental Limitations in the Measurement of Corona and Partial Discharge,” IEEE Transactions on Electrical Insulation, April 1982, Vol. EI-17, No. 2.

[12] R. J. Van Brunt, “Physics and Chemistry of Partial Discharge and Corona,” IEEE Transactions on Dielectrics and Electrical Insulation, October 1994, Vol. 1, No. 5, pp. 761-784.

[13] L. E. Lundgaard, “Partial Discharge-Part XIII: Acoustic Partial Discharge Detection-Fundamental Considerations,” IEEE on Electrical Insulation Magazine, July-Aug. 1992, Vol. 8, Issue. 4, pp. 25-31.

[14] L. E. Lundgarrd, “Partial Discharge-Part XIV: Acoustic Partial Discharge Detection-Practical Application,” IEEE on Electrical Insulation Magazine, Sep.-Oct. 1992, Vol. 8, Issue. 5, pp. 34-43.

[15] Wu Yan-kun, Yu Yan-long, Wu Ju-zhen, Wang Wei, Wang Zan, Bai Hong-wei and Huang Xiao-long, “Application of Acoustic-Optical Partial Discharge Detection in Power Cable,” Power System and Clean Energy, Aug. 2011, Vol. 27, No. 8, pp. 7-13.

[16] Brian Culshaw, “Acoustic Sensitivity of Optical-Fiber Waveguides,” Electronics Letters, Dec. 1977, Vol. 13, Issue. 25, pp. 760-761.

[17] J. A. Cosgrave, A. Vourdas, G. R. Jones, J. W. Spencer, M. M. Murphy, A. Wilson, “Acoustic Monitoring of Partial Discharges in Gas Insulated Substations Using Optical Sensors,” IEE Proceeding A-Science, Measurement and Technology, Sep. 1993, Vol. 140, Issue. 5, pp. 369-374.

[18] F. Y. Chu, “SF6 Decomposition in Gas-Insulated Equipment,” IEEE Transactions on Electrical Insulation, Oct. 1986, Vol. EI-21, Issue. 5, pp. 693-725.

[19] Sukhbir Singh, M. N. Bandyopadhyay, “Dissolved Gas Analysis Technique for Incipient Fault Diagnosis in Power Transformers: A Bibliographic Survey,” IEEE on Electrical Insulation Magazine, Nov.-Dec. 2010, Vol. 26, Issue. 6, pp. 41-46.

[20] N. C. Sahoo and M. M. A. Salama, “Trends in Partial Discharge Pattern Classification: A Survey,” IEEE Transactions on Dielectrics and Electrical Insulations, April 2005, Vol. 12, No. 2, pp. 248-264.

[21] C. H. Zhang and J. M. K. MacAlpine, “A Phase-related Investigation of AC Corona in Air,” IEEE Transactions on Dielectrics and Insulation, April 2003, Vol. 10, No. 2, pp. 312-319.

[22] Van Brunt, Richard J., “Physics and Chemistry of Partial Discharge and Corona - Recent Advances and Future Challenges,” IEEE Trans. on Dielectrics and Electrical Insulation, Vol. 1, Issue. 5, pp. 761-784.

[23] Alexander Belkov, Alija Obralic, Wojciech Koltunowicz and Ronald Plath, “Advanced Approach for Automatic PRPD Pattern Recognition in Monitoring of HV Assets,” IEEE International Symposium on Electrical Insulation, 6-9 June 2010, pp. 1-5.

[24] A. Cavallini, M. Conti, A. Contin and G. C. Montanari, “Advanced PD Inference in On-Field Measurements. Part 2: Identification of Defects in Solid Insulation Systems,” IEEE Transactions on Dielectrics and Electrical Insulation, June 2003, Vol. 10, No. 3, pp. 528-538.

[25] C. Chang, Q. Su, “Analysis of Partial Discharge Patterns from a Rod to Plane Arrangement,” IEEE International Symposium on Electrical Insulation, Anaheim, CA USA, April 2-5, 2000, pp. 439-443.

[26] Douglas C Montgomery, Design and Analysis of Experiments (8th edition), Wiley, April 10, 2012.

[27] A. Cavallini, G. C. Montanari, A. Contin and F. Puletti, “A New Approach to the Diagnosis of Solid Insulation Systems Based on PD Signal Inference,” IEEE Electrical Insulation Magazine, March/April 2003, Vol. 19, No. 2, pp. 23-30.

[28] G. C. Montanari, A. Cavallini and F. Puletti, “A New Approach to Partial Discharge Testing of HV Cable Systems,” IEEE Electrical Insulation Magazine, January/February 2006, Vol. 22, No. 1, pp. 14-23.

[29] M. Hoof, R. Patsch, “Pulse-Sequence Analysis: a New Method for Investigating the Physics of PD-Induced ageing,” IEE Proc.- Sci. Meas. Technol., January 1995, Vol. 142, No. 1, pp. 95-101.

[30] C. Chang and Q. Su, “Memory Propagation of Negative Point-to-plane Corona under AC Voltage,” IEE Proc.-Sci. Mesa. Technol., May 2002, Vol. 149, No. 3, pp. 117-126.

[31] Rainer Patsch, Farhad Berton, “Pulse Sequence Analysis-a Diagnostic Tool Based on the Physics behind Partial Discharges,” Journal of Physics D: Applied Physics, January 2002, Vol. 32, No. 1, pp. 25-32.

[32] Hans-Gerd Kranz, “PD Pulse Sequence Analysis and its Relevance for On-site PD Defect Identification Evaluation,” IEEE Transactions on Dielectrics and Electrical Insulation, April 2005, Vol. 12, No. 2, pp. 276-284.

[33] R. Bartnikas, K. D. Srivastava, Power and Communication Cables, Wiley-Interscience, 1999.

[34] Shinji Komatsuzaki, Seiji Kojima, Akihito Hongo, Nobuo Takeda and Tateo Sakurai, “Embedded FBG Sensors and AWG-based Wavelength Interrogator for Health Monitoring of Composite Materials,” 16th International Conference on Composite Materials, 2007.

[35] Xiao Meng-ben, Xiong Yan-ling and Zhao Hong, “A Fiber Bragg Grating Strain Sensor Based on ASE Light Source Demodulation Technology,” Journal Harbin Univ. SCI. & TECH., Feb. 2006, Vol. 11, No. 1, pp. 30-35.

[36] Nobuaki Takahashi, Kazuto Yoshimura, Sumio Takahashi and Kazuo Imamura, “Development of an optical Fiber Hydrophone with Fiber Bragg Grating,” Ultrasonics, 2000, pp. 581-585.